

## The Tropical Atmospheric Energy Budget from the TRMM Perspective. Part II: Evaluating GCM Representations of the Sensitivity of Regional Energy and Water Cycles to the 1998–99 ENSO Cycle

TRISTAN S. L'ECUYER AND GRAEME L. STEPHENS

*Department of Atmospheric Science, Colorado State University, Fort Collins, Colorado*

(Manuscript received 10 April 2006, in final form 19 October 2006)

### ABSTRACT

The impact of clouds and precipitation on the climate is a strong function of their spatial distribution and microphysical properties, characteristics that depend, in turn, on the environments in which they form. Simulating feedbacks between clouds, precipitation, and their surroundings therefore places an enormous burden on the parameterized physics used in current climate models. This paper uses multisensor observations from the Tropical Rainfall Measuring Mission (TRMM) to assess the representation of the response of regional energy and water cycles in the tropical Pacific to the strong 1998 El Niño event in (Atmospheric Model Intercomparison Project) AMIP-style simulations from the climate models that participated in the Intergovernmental Panel on Climate Change's (IPCC's) most recent assessment report. The relationship between model errors and uncertainties in their representation of the impacts of clouds and precipitation on local energy budgets is also explored.

With the exception of cloud radiative impacts that are often overestimated in both regions, the responses of atmospheric composition and heating to El Niño are generally captured in the east Pacific where the SST forcing is locally direct. Many models fail, however, to correctly predict the magnitude of induced trends in the west Pacific where the response depends more critically on accurate representation of the zonal atmospheric circulation. As a result, a majority of the models examined do not reproduce the apparent westward transport of energy in the equatorial Pacific during the 1998 El Niño event. Furthermore, the intermodel variability in the responses of precipitation, total heating, and vertical motion is often larger than the intrinsic ENSO signal itself, implying an inherent lack of predictive capability in the ensemble with regard to the response of the mean zonal atmospheric circulation in the tropical Pacific to ENSO. While ENSO does not necessarily provide a proxy for anthropogenic climate change, the results suggest that deficiencies remain in the representation of relationships between radiation, clouds, and precipitation in current climate models that cannot be ignored when interpreting their predictions of future climate.

### 1. Introduction

Regional differences in the character of clouds and precipitation play a significant role in defining the gradients of atmospheric heating that drive atmospheric circulations. The response of the character of clouds and precipitation to changes in their environment, therefore, plays a significant role in determining the impacts of global climate change. As a result, our ability to model the climate system and its response to natural and anthropogenic forcings requires a faithful represen-

tation of the complex interactions that exist between radiation, clouds, and precipitation and their influence on the large-scale energy balance and heat transport in the atmosphere. Since the first Atmospheric Model Intercomparison Project (AMIP I), which was initiated in 1989 (Gates 1992), much effort has been devoted to the problem of assessing parameterizations of these processes in climate models. Early results from this project indicated a number of notable errors in modeled fields such as a distinct cold bias, particularly over land and in polar regions (Boer et al. 1992; Mao and Robock 1998); errors in modeling the diurnal cycle of clouds (Groisman et al. 2000) and their radiative impacts on the atmosphere (Allen et al. 2002) and at the surface (Kleeman et al. 2001); varying degrees of difficulty in simulating intraseasonal and annual cycles of precipitation,

---

*Corresponding author address:* Dr. Tristan S. L'Ecuyer, Department of Atmospheric Science, Colorado State University, Fort Collins, CO 80523.  
E-mail: tristan@atmos.colostate.edu

particularly in regions characterized by strong moisture convergence (Srinivasan et al. 1995; Lau et al. 1996; Sperber and Palmer 1996; Gadgil and Sajani 1998); and an inability to predict the response of large-scale circulations to sea surface temperature (SST) forcings (Boyle 1998). Based on the ensemble of these and other studies summarized in Gates et al. (1999), it was suggested that flaws in the physical parameterizations employed by the models limited their utility for diagnosing key aspects of climate change. Soden (2000), for example, illustrates how differences between model and observation lead to ambiguities in important climate signals such as the response of the hydrologic cycle to greenhouse gas warming.

The second phase of the AMIP project, denoted AMIP-II and described in Glecker (1996), was completed in 2002 and demonstrated that many areas of model deficiency had been improved in the subsequent generation of GCMs. Kharin et al. (2005), for example, find that many of the AMIP-II models generated temperature extremes in good agreement with observations. Their results also suggest, however, that precipitation extremes are generally poorly represented, particularly in the Tropics where the influence of convective parameterizations dominates. The importance of such errors was further emphasized in the study by Fekete et al. (2004), who show that discrepancies between different monthly precipitation datasets including estimates from AMIP-II can lead to significant errors in hydrologic models of surface runoff.

Recently the Intergovernmental Panel on Climate Change (IPCC) has undertaken a new model intercomparison project to examine the performance of the latest generation of GCMs in preparation for their Fourth Assessment Report (AR4). The primary purpose of this study is to generate an ensemble of predictions of the future climate given a number of different scenarios of increasing atmospheric CO<sub>2</sub> concentrations. While it is important to assess the similarities and differences between distinct model realizations of these future climate scenarios, it is also critical to assess their response to shorter-term natural variability in environmental forcings using observations. This is the primary motivation behind the AMIP-style prescribed SST model integrations and forms the central focus of a number of recent studies as well as the present work. Preliminary results from the analysis of AMIP-style integrations from these models suggests that model physics have continued to improve in recent years. One notable example is the recent study of Wild et al. (2006) that chronicles the progress made in improving GCM representation of clear-sky shortwave absorption from the first AMIP simulations to the present. Overestimates of

surface shortwave fluxes relative to surface observations that exceeded 20 W m<sup>-2</sup> in some of the original AMIP models and averaged 4.5 W m<sup>-2</sup> in the AMIP-II integrations now average ~2.5 W m<sup>-2</sup> in the IPCC AR4 datasets. A key question that remains, however, is whether or not similar improvements have been made in modeling cloudy atmospheres.

It can be argued that a complete diagnosis of the physical processes at the root of discrepancies between model and observation requires simultaneous analysis of multiple components of the energy and water cycle in order to constrain as many aspects of the cloud–radiation–precipitation interaction as possible. Toward this goal, this paper seeks to evaluate the representation of basic components that govern regional energy and water cycles in the tropical Pacific in the IPCC AR4 models using a suite of satellite products generated by the multisensor algorithm developed in L'Ecuyer and Stephens (2003, hereafter Part I). The analysis focuses on the period between January 1998 and December 1999 representing to the two years of overlap between the AMIP model integrations and the Tropical Rainfall Measuring Mission (TRMM) satellite from which the observational data derive. Analysis of cloud–climate interactions during this period is also of particular interest since it encompasses the transition of SSTs in the Pacific Ocean from the strong 1997/98 El Niño event to the subsequent 1999 La Niña, eliciting a strong atmospheric response through associated changes in ocean–atmosphere energy transfer (L'Ecuyer et al. 2006). While this period is shorter than that analyzed in studies like that by Soden (2000) and is currently limited to oceanic regions, it nevertheless provides a natural example of a short-term climate change scenario in which clouds, precipitation, and regional energy budgets in the east and west Pacific are observed to respond to the eastward migration of warm SSTs. Furthermore, when compared with previous studies, the datasets analyzed here consist of a more extensive range of parameters including top-of-the-atmosphere (TOA) and surface radiative fluxes, clouds, precipitation, and geophysical parameters, such as SST and precipitable water all derived from the same platform, each with rigorous estimates of their uncertainties. These datasets provide a tighter constraint on model physics than can be realized with more limited subsets of parameters that often lack associated error estimates.

Section 3 characterizes the sensitivities of regional energy budgets in the tropical east and west Pacific to the 1998 El Niño from the observational perspective complete with a detailed discussion of associated uncertainty characteristics. Similar model-derived esti-

mates of atmospheric heating are compared to their TRMM-based counterparts in section 4. Finally, section 5 probes the sources of discrepancies between model and observation more deeply by examining the evolution of key geophysical parameters and atmospheric heating in the tropical east and west Pacific over the complete 1998/99 ENSO cycle. Particular emphasis is placed on the impact of condensed water on atmospheric heating through cloud radiative forcing and the release of latent heat.

## 2. Datasets

### a. Satellite products

The analysis that follows is based on products that have been generated using the approach outlined in Part I for estimating the spatial and temporal distribution of radiative fluxes and heating rates within the tropical atmosphere from TRMM observations. The technique, now known as the Hydrologic Cycle and Earth Radiation Budget (HERB) algorithm, synthesizes complementary ice cloud information from the Visible and Infrared Scanner (VIRS; Cooper et al. 2003), liquid cloud information from the TRMM Microwave Imager (TMI; Greenwald et al. 1993), and precipitation information from the TMI-based Goddard Profiling Algorithm (GPROF; Kummerow et al. 2000), to establish the three-dimensional structure of clouds and precipitation in the atmosphere. These fields are supplemented with profiles of temperature and humidity from European Centre for Medium-Range Weather Forecasts (ECMWF) analyses, ocean surface properties from Remote Sensing Systems (RSS), and a crude model of the global distribution of aerosol optical properties from the Global Aerosol Climatology Project (GACP) to obtain estimates of the primary factors that influence the propagation of radiation through the atmosphere. This, in turn, serves as input to a broadband radiative transfer model to compute upwelling and downwelling longwave (LW) and shortwave (SW) radiative flux profiles for each pixel. The model, known as BUGSrad, accounts for the effects of scattering, absorption, and emission from four hydrometeor classes that include cloud and precipitating modes of both liquid and ice hydrometeors. Computed flux profiles are subsequently used to derive principal components of the radiation budget and their breakdown into clear-sky and cloudy components. In the case of precipitating pixels, a crude estimate of column-integrated latent heating (LH) is also made assuming  $LH = \rho_l L_v R$ , where  $\rho_l$  is the density of liquid water,  $L_v$  is the latent heat of vaporization, and  $R$  is the retrieved surface rainfall rate. This relationship is only justified on spatial and tempo-

ral scales large enough to represent the complete life cycle of precipitating cloud systems, a good assumption for the large regions and monthly averages considered here.

After careful examination of all sources of error in the approach, Part I concludes that monthly mean LW fluxes at one-degree resolution are modeled to an accuracy of  $10 \text{ W m}^{-2}$ , with uncertainties dominated by the lack of ice cloud vertical placement information in the VIRS observations and errors in the vertical distribution of water vapor, particularly in the upper troposphere. Uncertainties in corresponding SW fluxes are on the order of  $25 \text{ W m}^{-2}$  and are dominated by errors in the detection of low clouds and poorly constrained liquid cloud microphysical properties. These estimates are consistent with comparisons of outgoing LW and SW flux estimates to observations from the Clouds and the Earth's Radiant Energy System (CERES) instrument (Wielicki et al. 1996) that indicate root-mean-square differences in monthly one-degree products of 8 and  $21 \text{ W m}^{-2}$ , respectively. For more details concerning the implementation of the HERB algorithm or the origins of these uncertainty estimates the reader is referred to Part I.

This study focuses on the time period between 1 January 1998 through 31 December 1999. Three oceanic regions between  $10^\circ\text{N}$  and  $10^\circ\text{S}$  are considered: the tropical west Pacific (TWP:  $105^\circ\text{--}150^\circ\text{E}$ ), tropical east Pacific (TEP:  $120^\circ\text{--}90^\circ\text{W}$ ), and a larger equatorial Pacific (EP) region that extends from  $105^\circ\text{E}$  to  $90^\circ\text{W}$  encompassing both of the smaller regions. The TRMM 1B01 VIRS calibrated radiance product supplies the 10.8- and 12- $\mu\text{m}$  brightness temperatures ( $T_B$ ) used to determine ice cloud properties, while low cloud retrievals make use of vertically and horizontally polarized  $T_B$  from the TMI 1B11 product. Liquid and ice water content profiles for precipitating systems are constrained using the TMI-based 2A12 TMI profiling product. Detailed descriptions and access to each of these datasets is provided by the Goddard Distributed Active Archive Center (DAAC; <http://daac.gsfc.nasa.gov/data/datapool/TRMM/index.html>). Vertical profiles of temperature and specific humidity for each  $0.25^\circ$  pixel are interpolated from 6-hourly,  $\sim 0.5^\circ$  analyses from ECMWF, while SST and precipitable water (CWV) fields from RSS are used to define the surface temperature and constrain the total column water vapor in each profile.

Figure 1 presents the evolution of TRMM-derived SST, CWV, high cloud fraction (HCF), and surface rainfall averaged from  $10^\circ\text{N}$  to  $10^\circ\text{S}$  for the analysis period. The transition from anomalously warm SSTs in the east and central Pacific in early 1998 to anomalously cool SSTs later in that year and throughout most of

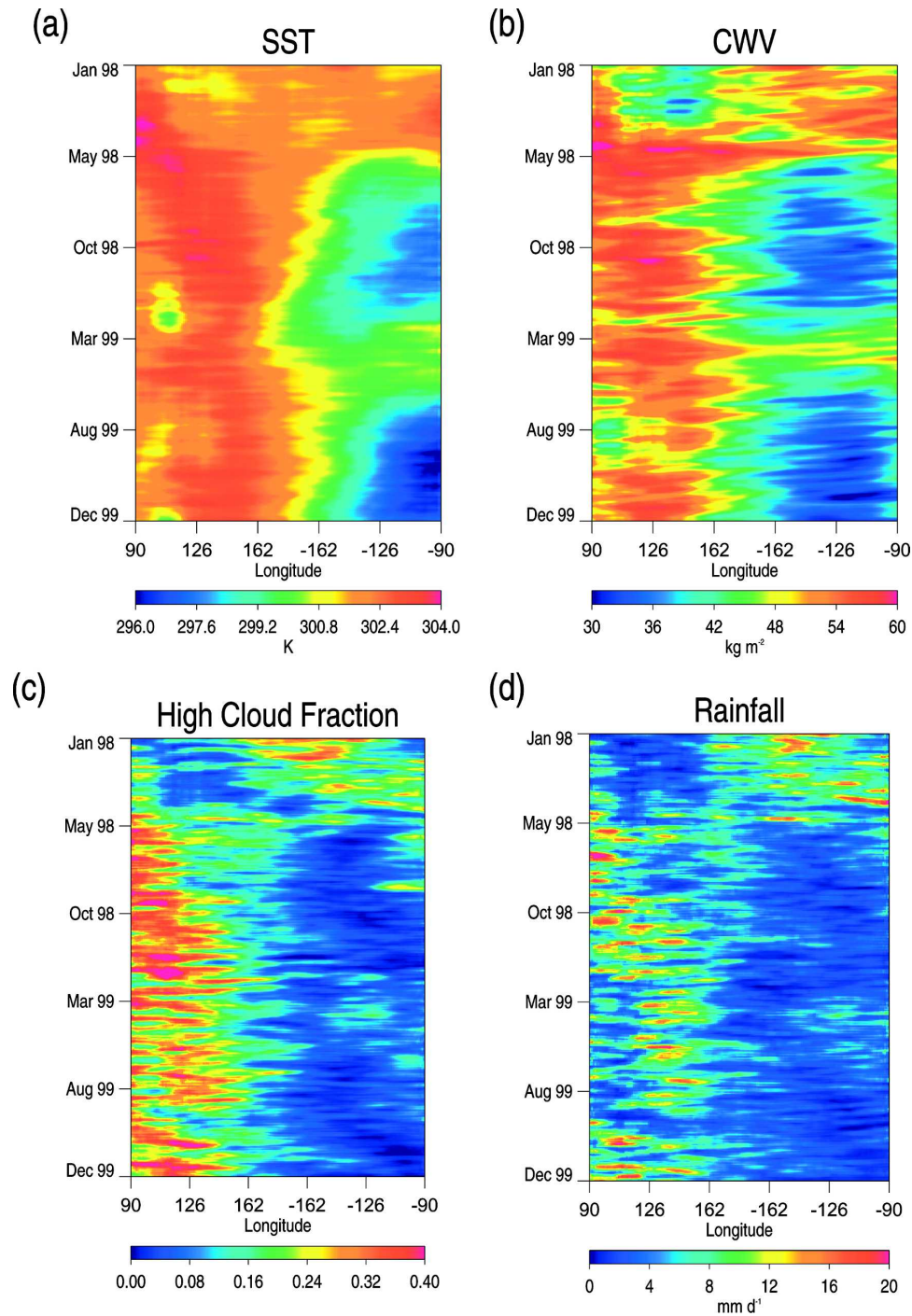


FIG. 1. The evolution of (a) SST, (b) precipitable water, (c) high cloud fraction, and (d) surface rainfall averaged from 10°N to 10°S for January 1998–December 1999.

1999 associated with the evolution of the ENSO is clearly evident. Also evident is a marked response in each of the other three fields to these changes in SST. CWV, for example, increases dramatically in the east Pacific during the first five months of 1998. More inter-

esting is the substantial drying that occurs in the west Pacific during this period despite the relatively small decrease in SST in the region. This suggests that a period of subsidence may have existed in the normally vigorously convective west Pacific during the 1998 El

TABLE 1. Summary of the models examined, the centers where they are employed, and associated references [adapted from Wild et al. (2006) and online documentation found at <http://www-pcmdi.llnl.gov/>]. Note that, while these are all coupled ocean–atmosphere models, the data analyzed here derive solely from their atmospheric components.

Model	Center	Reference
CNRM	Centre National de Recherches Meteorologiques, France	Deque et al. (1994)
ECHAM5	Max-Planck-Institut für Meteorologie, Germany	Roeckner (2003)
INM CM3	Institute for Numerical Mathematics, Russia	Galin et al. (2003)
IPSL CM4	Institut Pierre Simon Laplace, France	Marti et al. (2005)
MIROC-m	Center for Climate System Research, Japan	Hasumi and Emori (2004)
MIROC-h	Center for Climate System Research, Japan	Hasumi and Emori (2004)
CCSM3	National Center for Atmospheric Research, United States	Collins et al. (2006)
UKMO	Hadley Centre for Climate Prediction and Research, United Kingdom	Gordon et al. (2000)
CGCM2	Canadian Centre for Climate Modeling and Analysis, Canada	Flato (2005)

Niño. Many of these features are also evident in HCF and rainfall that, together, provide a proxy for the location of convection in the region. An eastward shift in convection clearly coincides with the eastward propagation of warm SSTs. It should be noted that the fields become progressively noisier in going from Fig. 1a to Fig. 1d. The more variable nature of fields like HCF and rainfall introduces an additional challenge when attempting to analyze model output. As a result, while an optimal strategy for evaluating model physics would involve intercomparisons at the smallest scales that can reasonably be resolved by both model and data, we are, in practice, limited to a more statistically based analysis of larger regions and longer integration periods. The analysis that follows is restricted to time scales ranging from monthly to annual and spatial scales  $5 \times 10^4 \text{ km}^2$  and larger.

### b. Models

Modeled geophysical parameters and radiative fluxes employed in this study derive from the most recent incarnation of a number of GCMs from the major international modeling groups that participated in the IPCC's Fourth Assessment Report. This set of model output, which can be obtained from the Program for Climate Model Diagnosis and Intercomparison (PCMDI) Web site (<http://www-pcmdi.llnl.gov/>), not only reflects the latest advances in global climate models but also constitutes the only widely available AMIP-style model intercomparison that overlaps the TRMM observation period. While 19 models had submitted data at the time of writing (March 2006), the nature of the comparisons that follow requires that the analysis be limited to those models for which upwelling and downwelling LW and SW fluxes at both the surface and TOA were available for both clear and cloudy skies to establish complete radiation budget estimates. A pared-down list of the nine IPCC AR4 models that meet this requirement is

provided in Table 1 along with the institutions where they were run, their spatial resolution, and references providing a detailed description of each model. The interested reader is directed to these references and the PCMDI Web site (<http://www-pcmdi.llnl.gov/>) for further information on the individual models analyzed. Despite being restricted to half of the models that participated in the IPCC AR4 intercomparisons, the data represent the models in use at the leading centers from seven different countries and thus provide a broad cross section of the current “state of the art” in climate modeling. It should be emphasized, however, that, while all participating models have coupled oceans, the nature of the forced-SST simulations analyzed here is such that only the atmospheric component of the models is evaluated. This has the advantage of ensuring that both model and observational datasets correspond to atmospheres that experience identical SST forcings and removes the additional degree of complexity introduced by variations in oceanic properties that cannot be adequately addressed with the limited observational time period examined here.

### 3. Observed regional energy budgets

The observed annual mean atmospheric energy budget for all oceanic pixels sampled by TRMM during 1998 and 1999 in the equatorial Pacific region is summarized in Fig. 2. Uncertainty estimates based on the analysis of Part I are also provided. Since it is not possible to determine the fraction of these errors that can be ascribed to random and systematic components, no reduction of noise through spatial and temporal averaging can be rigorously justified at this time: so the estimates provide an upper bound on the uncertainties in each quantity even though direct comparisons with CERES observations suggest that TOA fluxes are likely a factor of 2 more accurate than indicated. The

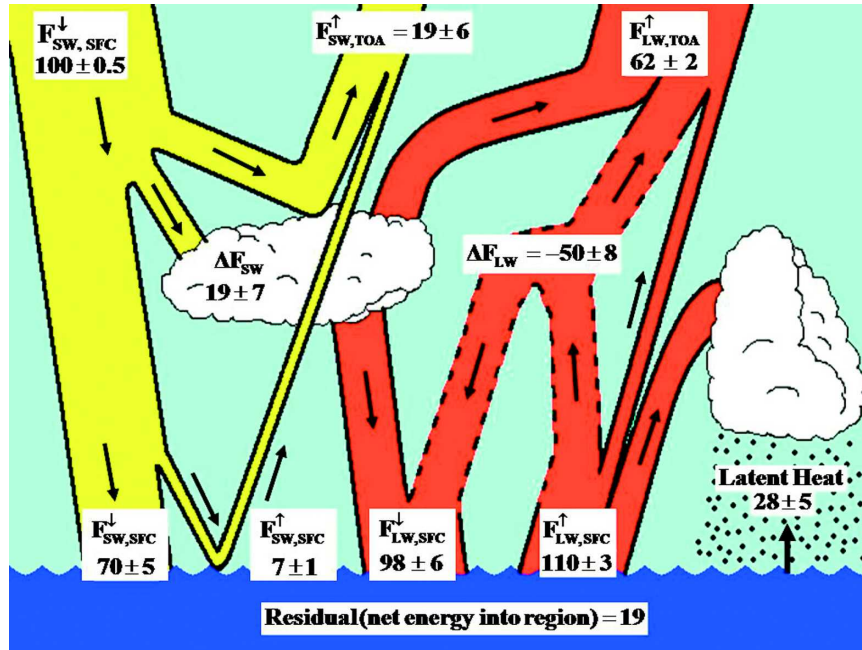


FIG. 2. Principal components of the atmospheric energy budget over oceanic regions between 10°N and 10°S, 105°E and 90°W averaged over the period from January 1998 through December 1999. All fluxes have been normalized by the mean solar insolation at TOA: 416 W m<sup>-2</sup>. Quoted uncertainties provide a maximum bound on the errors in each quantity based on the analysis conducted in Part I.

observations suggest that the combined albedo of the atmosphere, clouds, and surface is 19% and a total atmospheric absorption of 19% leaving 62% of the 416 W m<sup>-2</sup> incident at the top of the atmosphere to be absorbed at the ocean surface. At thermal wavelengths the atmosphere loses 207 W m<sup>-2</sup>, 116 W m<sup>-2</sup> of which is balanced by latent heat release in the atmosphere. When combined, these observations suggest that the atmosphere in the region is in approximate thermal balance experiencing only a small deficit of 12 W m<sup>-2</sup> that falls within the uncertainties of the products.

Implicit in Fig. 2 is the strong dependence of all quantities on the distribution of water between the atmospheric reservoirs of ice, liquid, and vapor. Beyond the obvious connection through latent heat released in phase changes, clouds arguably exert the strongest transient influence on radiative heating, increasing the planetary albedo and enhancing the absorption of SW radiation as well as trapping thermal radiation emitted from the surface. Of equal importance to the problem of modeling climate change are the reciprocal impacts of atmospheric diabatic heating on the generation and characteristics of new cloud and precipitation systems through its influence on local atmospheric dynamics. These impacts have been the focus of numerous studies on scales ranging from those of individual mesoscale

convective systems (e.g., Houze 1982, 1989; Mapes and Houze 1995), intraseasonal oscillations (e.g., Lau and Peng 1987; Lee et al. 2001), and the strength of the Hadley circulation (e.g., Slingo and Slingo 1988, 1991) and Walker circulation (e.g., Hartmann et al. 1984; Sherwood et al. 1994). The common conclusion to be drawn from these studies is the importance of accurately representing the factors that govern the mutual interactions between the atmospheric energy and water cycles in order to reliably represent the real-world behavior of most atmospheric processes.

Opportunities to create a complete observationally based representation of the large-scale atmospheric water budget from a single source have been limited, in part due to a lack of overlap between rainfall, cloud, and water vapor remote sensing within the satellite community. The instruments aboard the TRMM satellite, in combination with the HERB approach, not only make it possible to estimate all aspects of regional water cycles but also to provide rigorous estimates of the uncertainties in each individual component. A schematic representation of the distribution of water among its primary atmospheric reservoirs observed by TRMM over the same region and time period is presented in Fig. 3. Also identified are the primary pathways for exchanges between these reservoirs. Ice and liquid wa-

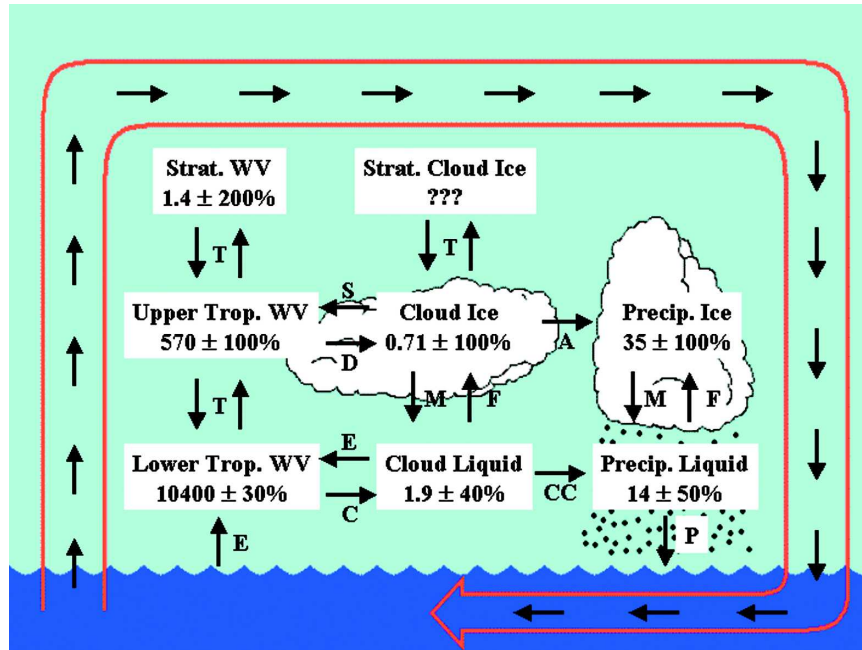


FIG. 3. Primary reservoirs in the hydrologic cycle over the tropical oceans for 1998. All water masses are in  $10^{12}$  kg. The lower troposphere is defined to extend from the surface to 500 mb, the upper troposphere from 500 to 200 mb, and the stratosphere above 200 mb. Arrows between reservoirs represent dominant pathways for exchange between them: evaporation (E), transport (T), condensation (C), deposition (D), sublimation (S), melting (M), freezing (F), aggregation (A), collision and coalescence (CC), and precipitation (P). Uncertainty estimates for precipitating liquid and ice derive from the analysis presented in L'Ecuyer and Stephens (2002). Those for cloud liquid and ice are from Greenwald et al. (1993) and Cooper et al. (2003), respectively. Uncertainties in ECMWF water vapor are adapted from Eyre (1990) and Eyre et al. (1993).

ter masses are integrated from the three cloud and precipitation algorithms described in Part I, the total mass of atmospheric water vapor is computed from RSS total precipitable water estimates, and its vertical distribution is determined from ECMWF analyses. The accompanying uncertainty estimates arise from rigorous analyses of the various algorithms and models from which each quantity derives: the interested reader is directed to the references listed in the figure caption for more details. Again, due to the lack of information regarding their breakdown into random and systematic components, the quoted error estimates should be viewed as upper bounds on potential errors in each product. The large magnitudes of these error estimates emphasize that our ability to quantify the atmospheric water reservoirs remains rather crude, particularly when it comes to ice and upper-tropospheric water vapor.

Water vapor makes up 99.5% of the water found in the atmosphere with 94% of that residing below 500 mb. The remaining atmospheric water exists as liquid water and ice, with precipitating hydrometeors ac-

counting for more than 10 times the mass of nonprecipitating liquid cloud droplets and ice particles. Despite accounting for less than half a percent of the atmospheric branch of the hydrologic cycle, however, water in its liquid and solid phases plays a crucial role in the energetics of the atmosphere. This is illustrated in Table 2, where the energy budget depicted in Fig. 2 is decomposed into components owing to precipitating, nonprecipitating cloudy, and clear-sky regions. The columns in Table 2 provide insight into the energy budgets of each type of pixel. Percentages that are larger (smaller) than the pixel fractions in the top row are indicative of flux components that are enhanced (reduced) in a particular hydrologic category relative to the mean state. Absorption and reflection of SW radiation, for example, are enhanced in clouds and precipitation, and a majority of the solar radiation that reaches the surface does so in clear-sky regions. Outgoing LW radiation (OLR) is reduced in all cloudy regions, but more so for nonprecipitating clouds, resulting in a significant reduction in atmospheric cooling. Finally, note that the release of latent heat is constrained to occur in

TABLE 2. Decomposition of the fluxes presented in Fig. 2 into three hydrologic categories: precipitating pixels (rain), nonprecipitating cloudy pixels (cloud), and clear-sky pixels (clear). The fraction of pixels that falls into each category is given in the top row. In subsequent rows, fluxes in the first column are expressed as percentages of the mean solar insolation at the top of the atmosphere,  $416 \text{ W m}^{-2}$ , while remaining columns provide the percentage of the total attributed to each pixel type.

Flux	Interpretation	Total	Rain	Cloud	Clear
$f$	Pixel fraction	100	15	19	66
$F_{\text{SW, TOA}}^{\downarrow}$	Incoming SW	100	15	16	69
$F_{\text{SW, TOA}}^{\uparrow}$	Outgoing SW	19	19	31	50
$\Delta F_{\text{SW}}$	SW absorption	19	17	17	66
$F_{\text{SW, SFC}}^{\downarrow}$	Downward SW at SFC	70	13	11	75
$F_{\text{LW, SFC}}^{\uparrow}$	Surface emission	110	15	19	66
$F_{\text{LW, SFC}}^{\downarrow}$	Downward LW at SFC	98	16	20	65
$\Delta F_{\text{LW}}$	LW deficit	-50	15	16	70
$F_{\text{LW, TOA}}^{\uparrow}$	Outgoing LW	62	14	15	71
LH	Latent heat	28	100	0	0

precipitating cloud systems since clouds that never precipitate eventually evaporate, ultimately canceling the latent heat released during their formation. Longwave radiative cooling, on the other hand, is maximum in clear-sky regions, implying that, while LH release may act to balance radiative cooling in an average sense, there are large imbalances on regional scales that have important implications for large-scale atmospheric dynamics.

Given the relatively short-term nature of the products analyzed here, deeper insights into fundamental connections between the energy and water cycles require the analysis of smaller regions and shorter time periods where signals are larger and can be more easily distinguished from noise in the observations and models. This is illustrated in Fig. 4, where heat budgets consisting of latent heating, shortwave radiative heating, and longwave radiative cooling are presented for the three regions defined above for the months of February 1998, representative of strong El Niño conditions, and February 1999, which corresponds to the subsequent weaker La Niña conditions that prevailed for much of 1999. Clearly the higher SSTs during El Niño lead to a net increase in the mean precipitation across the entire EP. As a result, the atmospheric energy balance that is realized over the full 2-yr period in fact results from a cancellation of a net heating that occurs during the El Niño and a cooling that occurs during La Niña periods.

The magnitude of the atmospheric response to ENSO is even larger when the TEP and TWP regions are examined separately. Variability in cloud radiative and latent heating between the two periods is more

than twice as large over these smaller regions than the EP as a whole. During February 1999, and during other periods characterized by average SST gradients across the Pacific, the atmosphere in the TWP is dominated by latent heat release that is more than twice as strong as the net radiative cooling in the region, creating a surplus heating of  $\sim 0.7 \text{ K day}^{-1}$  across the region. Conversely, the east Pacific loses energy at a rate of  $\sim 0.65 \text{ K day}^{-1}$  due to the predominance of radiative cooling and a lack of compensating latent heat release in precipitation. Thus, in a normal year, energy must be transported eastward out of the TWP, driving the zonal Walker circulation. When warmer SSTs propagate eastward with the onset of an El Niño event, however, the character of these regions changes dramatically, as illustrated by the left-most pair of heat budgets in Fig. 4. Warmer SSTs drive enhanced convection in the east Pacific apparently at the expense of that in the west. The resulting enhanced latent heat release coupled with reduced longwave radiative cooling that accompanies the associated high cirrus anvils leads to a net heating in the TEP region of almost  $0.8 \text{ K day}^{-1}$ , while the TWP cools at a rate of  $0.7 \text{ K day}^{-1}$ . The need to establish energy balance in these regions has the appearance of a circulation in the opposite direction that acts to suppress convection and in the TWP. This is, in fact, consistent with the large region of dry air in the TWP (Fig. 1) that is indicative of drying by subsidence in the region. While a qualitative understanding of the connection between ENSO and the Walker circulation was provided as early as the works of Bjerknes (1969), Cornejo-Garrido and Stone (1977), and Julian and Chervin (1978), quantitative estimates of the magnitudes of radiative and latent heating on temporal and spatial scales large enough to be comparable to those characteristic of climate models have only become possible in the satellite era due to multisensor products like those from the HERB algorithm. With the results presented thus far as a backdrop, the remainder of this paper will assess the representativeness of the IPCC AR4 climate models in the context of the conceptual models of the energy and water cycles depicted in Figs. 2 and 3.

#### 4. Modeled heat budgets

Two-year mean radiative fluxes over the EP region extracted from the nine IPCC AR4 models and those from the TRMM observational dataset are compared in Table 3. Longwave fluxes are generally well represented by all models with differences on the order of  $10 \text{ W m}^{-2}$ , comparable in magnitude to the accuracy of the observations. As a result, all datasets predict long-

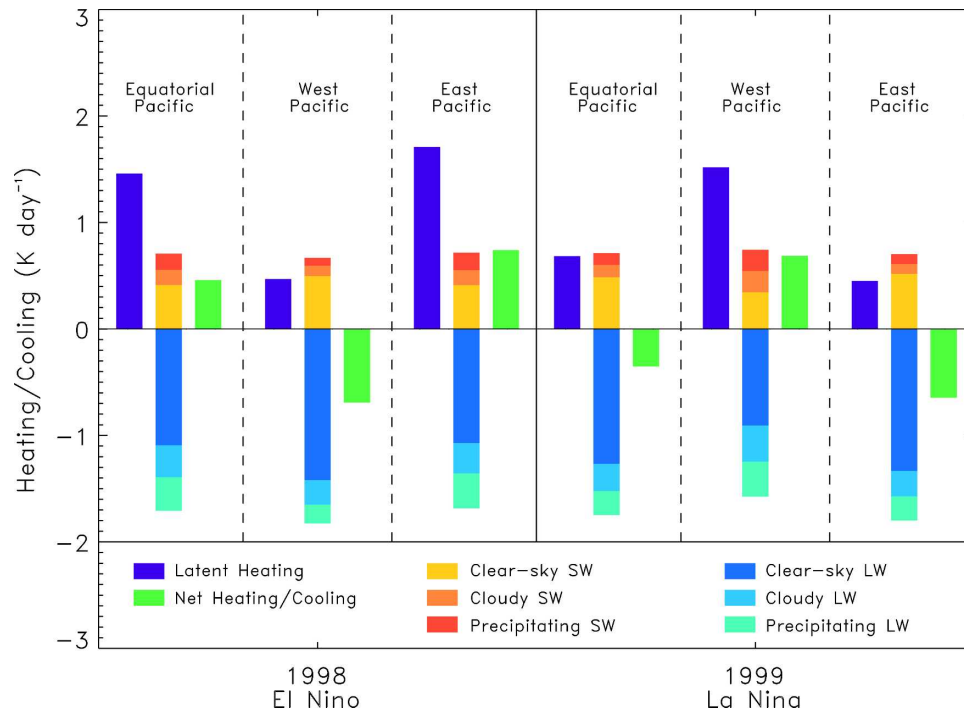


FIG. 4. Atmospheric heat budgets during February 1998 and February 1999 for the full equatorial Pacific and smaller east and west Pacific regions. For each region and each month the left-most bar (purple) indicates the contribution of latent heating, the middle bar presents the contributions of clear-sky, nonprecipitating cloudy, and precipitating pixels to the total shortwave radiative heating (warm colors) and longwave radiative cooling (cool colors), and the bar on the right (green) presents the net heating or cooling in the region due to the sum of all of these contributions.

wave radiative cooling in the region consistent to within  $\pm 5\%$  of  $1.6 \text{ K day}^{-1}$  and there is no evidence of any uniform bias on either side of the observations. Conversely, modeled latent heat release in the atmosphere, derived from surface rainfall estimates in a manner consistent with that adopted in the HERB algorithm (section 2), is systematically higher than observed. The L'Institut Pierre-Simon Laplace Coupled Model version 4 (IPSL CM4) and Coupled General Circulation

Model version 2 (CGCM2) provide the closest match to observations, yielding estimates within 10% of the TRMM observations, while the Model for Interdisciplinary Research on Climate (MIROC) models overestimate latent heating by  $\sim 25\%$ . These differences are, however, only slightly larger than those that arise when version-5 monthly rainfall datasets from the TMI and Precipitation Radar (PR) instruments aboard TRMM (3A12 and 3A25, respectively) are compared for the

TABLE 3. Mean observed and modeled values of the principal radiative and latent heat fluxes over the equatorial Pacific region averaged over the period from January 1998 to December 1999. As in Fig. 1, all fluxes are normalized to the mean solar insolation at TOA:  $416 \text{ W m}^{-2}$ .

Source	$F_{\text{SW, TOA}}^{\downarrow}$	$F_{\text{SW, TOA}}^{\uparrow}$	$\Delta F_{\text{SW}}$	$F_{\text{SW, SFC}}^{\downarrow}$	$F_{\text{LW, SFC}}^{\uparrow}$	$F_{\text{LW, SFC}}^{\downarrow}$	$\Delta F_{\text{LW}}$	$F_{\text{LW, TOA}}^{\uparrow}$	LH
TRMM	100	19	19	70	111	98	-50	62	28
CNRM	100	27	24	52	112	100	-49	61	35
ECHAM5	100	23	22	60	112	100	-48	60	34
INM CM3	100	21	23	61	112	100	-47	59	33
IPSL CM4	100	23	21	61	112	97	-46	61	29
MIROC-h	100	24	24	54	112	98	-46	59	36
MIROC-m	100	28	25	49	112	100	-45	58	36
CCSM3	100	25	23	54	112	101	-48	59	32
UKMO	100	20	14	62	112	99	-51	64	33
CGCM2	100	25	23	58	112	100	-48	60	31

same region. The results, therefore, indicate that the nine GCMs examined reproduce the mean longwave fluxes and atmospheric latent heat release in the EP region to within the accuracy of the TRMM observations.

Discrepancies in modeled and observed SW fluxes are more significant. Models predict both a brighter atmosphere, indicated by larger mean outgoing SW radiation (OSR) and, with the exception of the Met Office (UKMO) model, a more absorbing atmosphere than the observations indicate. In most cases, the differences in observed and simulated atmospheric absorption are  $\sim 10\text{--}15 \text{ W m}^{-2}$ , within the uncertainty estimates of HERB products. With the exception of the Centre National de Recherches Météorologiques (CNRM) and MIROC models, discrepancies in OSR are similar within observational error bounds, but the fact that modeled atmospheres both reflect and absorb more solar radiation than the observations leads to significant discrepancies in the total downwelling SW radiation at the surface (SSR) that range from 32 to  $80 \text{ W m}^{-2}$ . The results also imply that the models themselves exhibit disparities of almost  $50 \text{ W m}^{-2}$  in their estimates of the solar radiation reaching the earth's surface. The source of these discrepancies can almost undoubtedly be traced to challenges in modeling the propagation of SW radiation in cloudy atmospheres. Given the sensitivity of cloud albedo to their spatial distribution, three-dimensional structure, and ice crystal shape coupled with the fact that this region is characterized by large concentrations of high clouds associated with deep convection, it is not surprising that the SSR is the most poorly characterized flux in the IPCC AR4 GCMs. It is also important to note that the myriad of assumptions required in modeling SSR also likely result in large uncertainties in satellite-derived SSR. It will be demonstrated below, however, that some models appear to generate more clouds than observed in the independent International Satellite Cloud Climatology Project (ISCCP) dataset supporting the assertion that modeled atmospheres may absorb and, especially, reflect too much SW radiation.

The primary drawback to analyzing large regions and long time periods is the natural tendency for uncertainties in regions with different large-scale dynamics to cancel one another. This is particularly true in the equatorial Pacific, which encompasses both ascending and descending branches of the Walker circulation. Far greater insights into model performance can be gleaned when the EP region is decomposed into the smaller TWP and TEP regions and when El Niño periods are distinguished from those characterized by La Niña conditions. Figure 5 presents atmospheric heat budgets in

the TWP and TEP regions from the IPCC AR4 models and TRMM observations, focusing again on the months of February 1998 and 1999. Each panel presents LW cooling, latent heating, and SW heating in the form of bars along with a corresponding estimate of the net heating resulting from the sum of these components in parentheses at the base of the plot. Corresponding geophysical parameters are summarized in Tables 4 and 5 for the TWP and TEP regions, respectively.

Despite the differences in SW fluxes noted above, Fig. 5 clearly indicates that differences in net heating are primarily driven by variations in the imbalances in LW cooling and latent heating estimates among models. There is a general consensus among models and the TRMM products that the TEP region evolves from one characterized by strong net cooling in normal years to one with strong net heating during the 1998 El Niño. More than half of the models simulate net heating rates in February 1998 that are within 20% of the observed  $0.74 \text{ K day}^{-1}$ , within the error bars on the TRMM data. From Table 5, these models also generally agree that the subsidence generally characteristic of the TEP is replaced with weak large-scale ascent during the El Niño period. In addition, precipitable water increases by  $\sim 20\%$  and surface rainfall generally increases by a factor of 2 or 3. There are, however, notable exceptions such as the IPSL CM4 and CGCM2 models that significantly underestimate the increase in east Pacific rainfall during El Niño, leading to dramatically lower estimates of net atmospheric heating in the region.

These examples aside, there is much better consensus between the IPCC AR4 GCMs and the TRMM observations in the TEP than in the TWP where models exhibit widely varying responses to El Niño. The TRMM products predict a significant decrease in latent heat release by precipitation and enhanced LW cooling during February 1998, resulting in a reversal of heating that mirrors that observed in the TEP. Of the nine models examined, however, only the UKMO, ECHAM5, and MIROC-m models simulate the observed cooling in the TWP during El Niño, and of these only the first two are of an appropriate magnitude. All others maintain a heating in the TWP ranging from 0.5 to  $1.0 \text{ K day}^{-1}$ . Interestingly, with the exception of IPSL CM4, model-derived LW radiative cooling rates are all within  $\sim 20\%$  of that observed. Similarly, with the exception of the UKMO model, atmospheric SW heating estimates span a range of only  $\sim 25\%$  about the HERB products. The vast majority of the differences in net heating can, therefore, be traced to variations in the latent heat release owing to significant differences in the modeled response of precipitation to El Niño, which varies by more than a factor of 4 between the

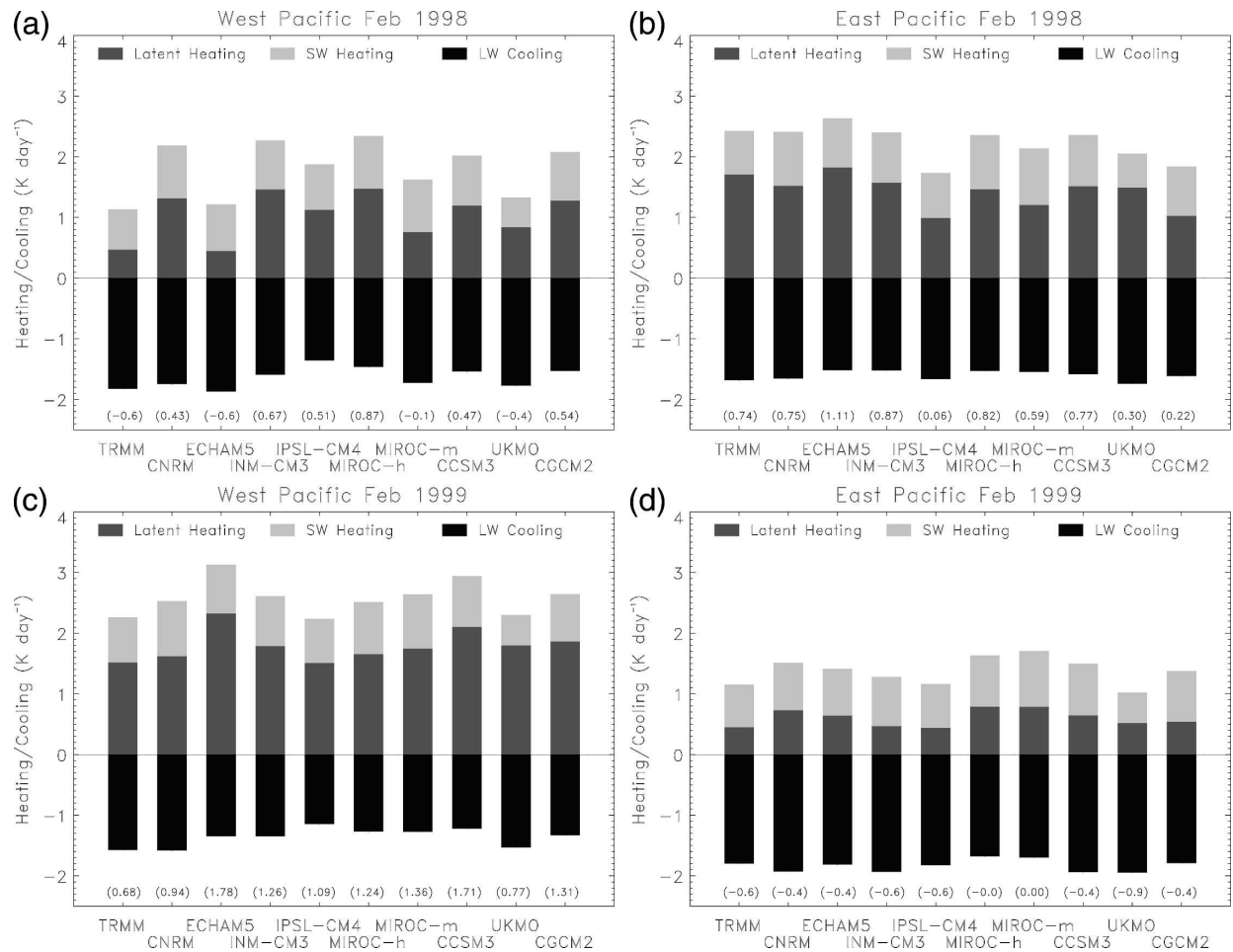


FIG. 5. Observed and modeled heat budgets for the TWP and TEP regions during February 1998 and February 1999. Net atmospheric heating estimates from the sum of all three components are provided in parentheses across the base of each plot.

driest and wettest models. These large discrepancies are consistent with differences in large-scale vertical motion among models. While all models reduce the magnitude of large-scale ascent in the TWP during the El Niño relative to La Niña conditions, only the MIROC-m and UKMO models actually generate subsidence in the region, which may be expected given the observed drying illustrated in Fig. 1. Under conditions of stronger east–west SST gradients, such as in February 1999, most models exhibit much better agreement with observed precipitation amounts and, therefore, net heating although there is once again a tendency for the models to generate too much precipitation in the region relative to TRMM observations. Unlike the El Niño period, there is also better consistency in model-simulated large-scale ascent in the TWP during February 1999.

Based on these results it is reasonable to conclude that a majority of the GCMs studied generally repre-

sent atmospheric properties and heating in both regions during periods of large east–west SST gradients characteristic of normal or La Niña conditions. The atmospheric response to the eastward propagation of warm SSTs associated with El Niño, however, is found to be more challenging. Although there are some exceptions, many models perform reasonably well in the TEP region where the influence of El Niño on local SST is largest, but there is a general failure to achieve consensus in the TWP region where the impacts of El Niño are manifested more indirectly through changes in the large-scale circulation across the Pacific. In fact the magnitude of the differences in modeled precipitation and heating in the TWP in February 1998 are comparable to the observed heating changes between 1998 and 1999, suggesting a fundamental lack of model skill in simulating changes in these parameters. Put another way, the ratio of signal to intermodel “noise” is  $\sim 1$ , implying that the ensemble provides no information re-

TABLE 4. Mean values of a number of geophysical parameters in the TWP region during February 1998 and 1999. Note that vertical motions at 500 mb, represented by  $\omega_{500}$ , are reported in pascals per second.

Source	SST (K)	CWV (kg m <sup>-2</sup> )	R (mm d <sup>-1</sup> )	$V_{sfc}$ (m s <sup>-1</sup> )	$\omega_{500}$ (Pa s <sup>-1</sup> )
Feb 1998					
TRMM	301.4	42.9	2.2	6.2	n/a
CNRM	301.5	51.9	6.1	3.7	-0.0081
ECHAM5	301.9	47.5	2.1	4.0	n/a
INM CM3	301.5	43.6	6.7	7.2	-0.0202
IPSL CM4	301.8	53.0	5.2	3.9	-0.0233
MIROC-h	301.4	46.7	6.8	3.0	-0.0335
MIROC-m	301.7	43.9	3.5	3.4	0.0032
CCSM3	301.6	49.7	5.5	n/a	-0.0185
UKMO	302.0	n/a	3.9	4.0	0.0048
CGCM2	301.7	46.9	5.9	3.4	-0.0255
Feb 1999					
TRMM	302.0	50.0	7.0	4.9	n/a
CNRM	301.7	58.2	7.5	2.2	-0.0307
ECHAM5	302.1	56.2	10.7	2.9	n/a
INM CM3	301.9	48.5	8.2	5.0	-0.0448
IPSL CM4	302.0	49.1	7.0	3.6	-0.0490
MIROC-h	301.8	47.3	7.6	2.1	-0.0540
MIROC-m	301.8	58.6	8.1	2.4	-0.0527
CCSM3	301.9	53.5	9.7	n/a	-0.0643
UKMO	302.1	n/a	8.3	3.1	-0.0420
CGCM2	301.9	49.8	8.6	2.8	-0.0603

garding the response of heating and precipitation in the TWP to El Niño.

## 5. Observed and modeled relationships between radiation, hydrology, and the local environment

While these two monthly “snapshots” provide significant insight into the performance of the IPCC AR4 GCMs, it is also of interest to examine the evolution of local atmospheric dynamic and thermodynamic properties over the complete ENSO cycle. To this end, this section analyzes data from the full 24-month dataset are used to provide a more rigorous comparison of observed and modeled relationships between atmospheric radiative heating, large-scale atmospheric properties, and the 1998–99 El Niño–La Niña cycle.

### a. Temporal evolution of radiative fluxes and geophysical parameters

Time series of several geophysical parameters in the TEP and TWP regions for the period from January 1998 through December 1999 are presented in Fig. 6, illustrating their evolution across a more or less complete ENSO cycle. To facilitate comparisons of trends, the 2-yr mean value of each parameter has been extracted and summarized in the legend at the right of

TABLE 5. As in Table 4, but for the TEP region.

Source	SST (K)	CWV (kg m <sup>-2</sup> )	R (mm d <sup>-1</sup> )	$V_{sfc}$ (m s <sup>-1</sup> )	$\omega_{500}$ (Pa s <sup>-1</sup> )
Feb 1998					
TRMM	301.9	50.2	7.9	5.8	n/a
CNRM	301.4	52.7	7.0	4.5	-0.0152
ECHAM5	302.0	58.6	8.4	2.8	n/a
INM CM3	301.9	48.2	7.2	6.7	-0.0268
IPSL CM4	301.9	52.2	4.6	3.4	-0.0783
MIROC-h	301.8	49.5	6.7	3.0	-0.0318
MIROC-m	301.8	50.7	5.6	3.4	-0.0180
CCSM3	301.9	53.2	7.0	n/a	-0.0305
UKMO	301.8	n/a	6.9	2.8	-0.0233
CGCM2	301.8	50.6	4.7	2.9	-0.0132
Feb 1999					
TRMM	299.5	42.3	2.1	3.6	n/a
CNRM	299.6	35.8	3.4	3.9	0.0215
ECHAM5	299.4	45.4	3.0	3.0	n/a
INM CM3	299.2	37.2	2.2	6.1	0.0210
IPSL CM4	299.5	40.4	2.0	3.0	0.0217
MIROC-h	299.4	41.8	3.6	2.5	-0.0010
MIROC-m	299.5	44.0	3.6	3.6	0.0022
CCSM3	299.5	44.5	3.0	n/a	0.0188
UKMO	299.5	n/a	2.4	4.6	0.0293
CGCM2	299.5	40.4	2.5	1.8	0.0147

each panel. The top panels demonstrate that the modeled and observed SST variations are nearly identical. The small differences (<0.5 K) between the model ensemble and TRMM dataset reflect sampling and methodology differences between the TRMM-based SST estimates from RSS (Wentz 1997) used in HERB and the Reynolds SSTs (Reynolds and Smith 1994) that constrain the models throughout the integrations analyzed here. With the exception of surface wind speed, which varies widely among models in both regions, there is generally much better agreement between models and observations in both the 2-yr means and trends of atmospheric properties in the TEP region where SST variability is largest. Mean precipitable water, for example, varies by less than 10% between models and measurements, and all sources agree that the TEP was more moist during the 1998 El Niño event than during other periods. Models and observations also agree that rainfall increased in the TEP region during the period of elevated SSTs in the region, although many models underestimate the magnitude of this increase relative to the TRMM observations. Finally, based on the vertical velocity at 500 mb, there is a general consensus among models that the region is characterized by large-scale ascent during the 1998 El Niño and subsidence at other times. It is, however, important to note that there is significantly more intermodel variability in both precipitation and  $\omega_{500}$ , reflecting the more indirect impact of SST on these quantities.

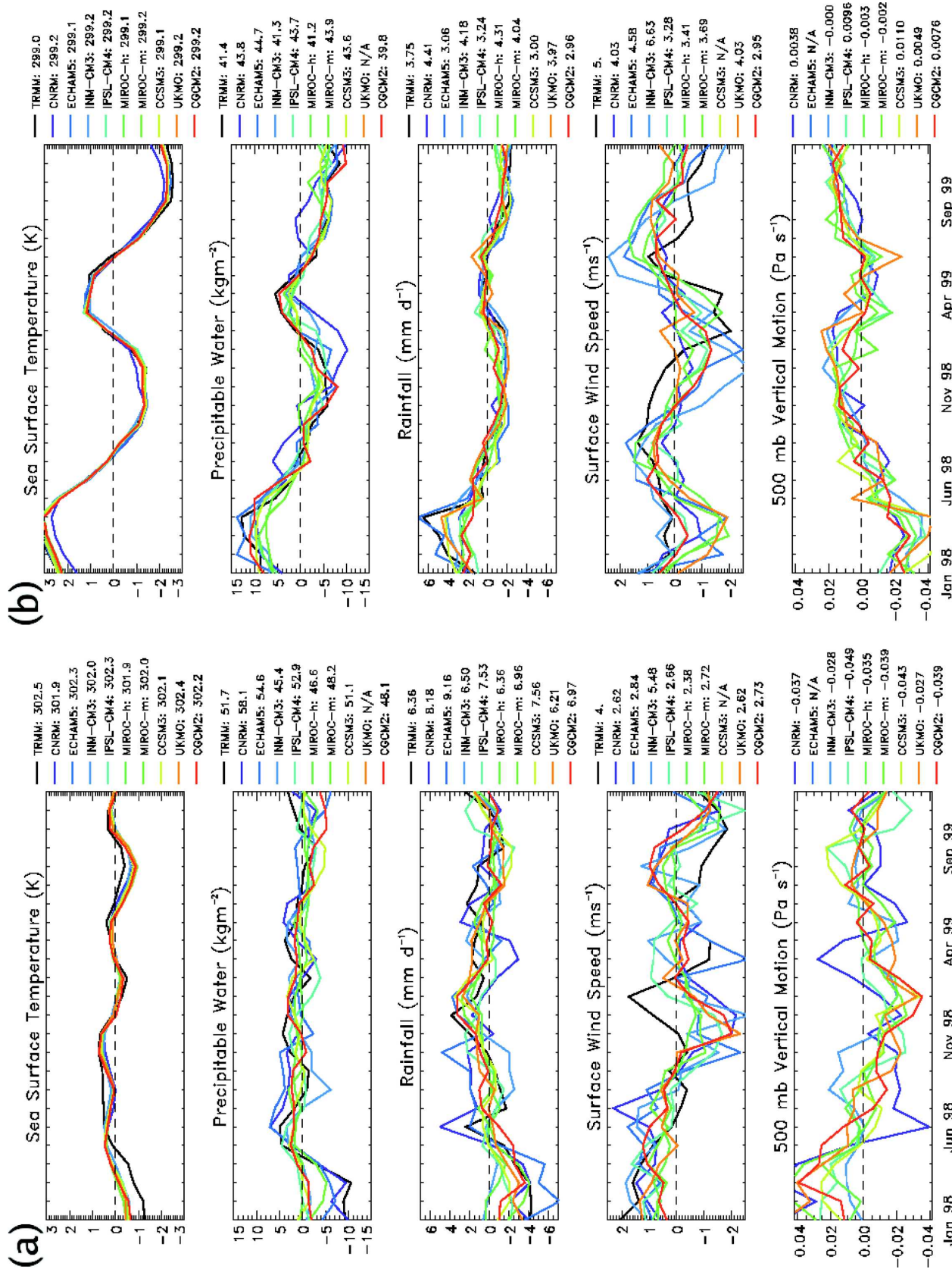


FIG. 6. Observed and modeled evolution of monthly mean SST, precipitable water, rainfall, surface wind speed, and large-scale vertical motion through the 1998 El Niño and 1999 La Niña periods in the (left) TWP and (right) TEP. Each panel displays trends about the 2-yr mean values summarized in the legend at the right.

Agreement between models and observations is far less convincing in the TWP region. Despite very similar SSTs, mean precipitable water over the period varies by more than 25% among models, while mean rainfall estimates span a range of 40%. There is also a lack of consensus among models regarding the trends in many parameters, and few capture the variability manifested in the TRMM observations. The Institute for Numerical Mathematics Climate Model version 3 (INM CM3) and IPSL CM4, for example, indicate very little change in rainfall during El Niño, while the CNRM and medium-resolution MIROC models predict decreases of more than 50%, in better agreement with observations. A very similar conclusion was reached by Lau et al. (1996) who note that intermodel precipitation variability is extremely large in regions that they term to be in strong dynamical control like the TWP. The fact that their findings grew out of the first AMIP model integrations suggests that, two generations later, GCMs continue to exhibit similar problems to those in use more than a decade ago, although there is evidence that agreement among models has improved outside the 1998 El Niño period. It is also worth noting that only the CNRM and ECHAM5 models capture the observed drying in the TWP in the first few months of 1998. All other models predict that precipitable water remains constant, perhaps an artifact of the very small SST variations throughout the period.

Of the five fields plotted,  $\omega_{500}$  is clearly the most variable among models. Two-year means vary by as much as 40%, while trends vary across a wide spectrum of amplitudes. The INM CM4, for example, indicates only a very slight decrease in large-scale ascent in the TWP during the 1998 El Niño while the MIROC-m and CNRM models predict anomalies large enough to induce weak subsidence in the early months of the time series. Noting that these models also reproduce observed trends in other fields, this suggests that it is more likely that a regime of weak subsidence prevailed in the TWP region during the first few months of 1998, consistent with the findings of Allen et al. (2002).

Following Stephens and Greenwald (1991), we characterize the LW radiative impact of clouds on their environment by their modification of the atmospheric greenhouse parameter,  $G$ , defined as the ratio of surface emitted LW flux to that emitted to space:

$$G_{\text{cld}} = \frac{\sigma T_s^4}{(F_{\text{LW,TOA}}^{\uparrow})_{\text{all sky}}} - \frac{\sigma T_s^4}{(F_{\text{LW,TOA}}^{\uparrow})_{\text{clear sky}}}, \quad (1)$$

where  $\sigma$  is the Stefan–Boltzmann constant and  $T_s$  represents surface temperature. Similarly, cloud SW impacts are measured by their modification of the albedo

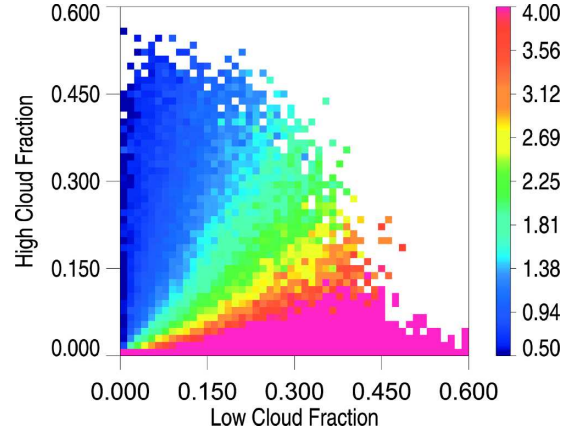


FIG. 7. Relationship between TOA cloud forcing ratio,  $N$ , and high and low cloud fraction from two years of TRMM observations for all oceanic pixels between 40°S and 40°N.

parameter,  $\alpha$ , which is the difference between the outgoing SW radiation at the TOA between the all-sky conditions that are observed and an equivalent pixel with all clouds and precipitation removed, normalized by solar insolation.

In addition to these parameters that isolate the LW and SW effects of clouds, it is also useful to examine the relative strength of these two effects. To this end, we also analyze the ratio of cloud impacts on TOA SW to LW fluxes,  $N$ , which has the benefit that values greater than (less than) unity are indicative of a net cooling (heating) effect in the atmosphere. This ratio, introduced by Kiehl (1994), who noted a near cancellation of cloud LW and SW impacts across large regions of the tropical Pacific, and later used by Cess et al. (2001) and Allen et al. (2002) to explore the response of cloud radiative impacts in the TWP to ENSO, can be defined in terms of the flux variables in Table 2 as

$$N = -1 \times \frac{(F_{\text{SW,TOA}}^{\uparrow})_{\text{clear sky}} - (F_{\text{SW,TOA}}^{\uparrow})_{\text{all sky}}}{(F_{\text{LW,TOA}}^{\uparrow})_{\text{clear sky}} - (F_{\text{LW,TOA}}^{\uparrow})_{\text{all sky}}}. \quad (2)$$

As opposed to  $G_{\text{cld}}$  and  $\alpha_{\text{cld}}$ , which are sensitive to high clouds and total cloudiness, respectively,  $N$  provides a direct measure of the relative fractions of low and high clouds in a region. This is illustrated in Fig. 7, where  $N$  is presented as a function of high and low cloud fraction. When shallower cloud systems prevail, the region will exhibit substantially more SW cooling than LW heating while an atmosphere containing a larger fraction of deep systems will trap an amount of LW radiation that is approximately equal to the SW radiation it reflects. In the context of global climate change, the sensitivity of  $N$  to changes in the environment is, in some sense, the critical response that determines

whether or not the global cloud radiative feedback is positive or negative.

Together  $N$ ,  $G_{\text{cld}}$ , and  $\alpha_{\text{cld}}$  provide sufficiently strong constraints to rigorously evaluate the representation of clouds and their radiative impacts in the IPCC AR4 GCMs. The evolution of each over 1998 and 1999 is presented in Fig. 8 for both the TWP and TEP. Focusing first on the average values of each parameter that is summarized on the right-hand side of each plot, there is a significant amount of intermodel variability in the mean cloud radiative effects in each region. Two-year mean values of  $N$ , for example, vary by  $\sim 40\%$  in the TWP and a factor of 2 in the TEP region, indicating significant differences in the relative frequency of high and low clouds among models. Furthermore, based on the mean values of  $G$  and  $\alpha$ , many models overestimate both LW and SW radiative impacts of clouds on their environment relative to observations. This suggests that either the number of clouds or their optical properties is misrepresented in the GCMs.

To narrow down the source of these discrepancies, modeled cloud fractions are compared to those quoted in the International Satellite Cloud Climatology Project (ISCCP) monthly cloud amount dataset for both regions in Fig. 9 [see Rossow and Schiffer (1991, 1999) for an overview of the ISCCP dataset]. In the TWP, most models either overestimate or underestimate mean cloud cover by at least 10% and as much as 17%. Only the Community Climate System Model version 3 (CCSM3) predicts similar mean cloudiness in the region. Models tend to simulate mean cloudiness in better agreement with ISCCP in the TEP region, although the CNRM and INM CM3 models still indicate  $\sim 15\%$ – $20\%$  more cloud cover than observed. Notice also that 2-yr mean cloud fraction varies between models by as much as 30%. The predicted sensitivity of cloud cover to ENSO is equally variable between models, although they generally agree with observations that there is a reduction (increase) in cloudiness in the TWP (TEP) during El Niño consistent with the observations. The amplitude of ENSO-related variability in TEP cloud cover is, for example,  $\sim 16\%$  in the CCSM3 model, while cloud amounts vary by more than 40% in both the CNRM and INM CM4 models. In the TWP, there are also significant differences in the timing of peaks in cloudiness. The CNRM model returns to “normal” cloud cover conditions in June 1998, almost immediately upon the termination of El Niño, while many others, such as MIROC and CCSM3, exhibit below-average cloudiness until December or January, in much better agreement with ISCCP. As might be expected, these differences also lead to discrepancies in the modeled response in cloud radiative impacts to ENSO.

Very few models, for example, capture the observed increase in  $N$  in the TWP during the 1998 El Niño.

Figure 8 also provides strong evidence that models disagree on the partitioning of total cloud cover into high and low clouds. Consider, for example, the INM CM3, which predicts some of the largest cloud fraction anomalies in the TEP region among the ensemble. This model also predicts the largest ENSO signal in  $G_{\text{cld}}$  and  $\alpha_{\text{cld}}$  but small changes in  $N$  relative to the others. This suggests that the relative frequency of occurrence of high and low clouds in the INM CM3 is not very sensitive to ENSO. Conversely, the CCSM3 generates the smallest signals in cloud amount, impact on  $G$ , and impact on  $\alpha$ , but some of the largest variability in  $N$ , implying a significant shift from high clouds during the warm SST period in early 1998 to predominantly low clouds later that year. When compared with the TRMM observations, which lie somewhere between these extremes, these results indicate that, in addition to errors in total cloud cover, it is also likely that the vertical placement and optical properties of modeled clouds are misrepresented in many models.

#### *b. Statistical relationships*

To more directly emphasize sensitivities to changes in SST conditions associated with ENSO, in Figs. 10 and 11 the relationships are explored between surface rainfall, cloud radiative effects, and the SST gradient between the TWP and TEP regions,  $\Delta = \text{SST}_{\text{TWP}} - \text{SST}_{\text{TEP}}$ , which serves as a proxy for the ENSO phase. Large values of  $\Delta$  correspond to La Niña conditions, while small or negative values represent El Niño events in the tropical Pacific. For reference, a SST gradient of  $\Delta \sim 4$  K is typical of average conditions in the Pacific. A subset of original models is isolated so as to span the range of model behavior while limiting unnecessary clutter in each panel.

Qualitative comparison of the results indicates that, while there is scatter in all fields in both regions, relationships are generally better defined and exhibit better agreement among the various sources of information in the TEP than in the TWP. The four models shown and the TRMM observations all indicate significant increases in precipitation and  $G_{\text{cld}}$  in the TEP under SST gradients typical of El Niño conditions. Cloud impact on albedo is generally invariant with  $\Delta$  but the magnitude varies by a factor of 3 between the models shown, with the INM CM3 predicting the smallest  $\alpha_{\text{cld}}$  in better agreement with the TRMM observations and the CNRM model indicating the largest. The ratio of cloud SW and LW impacts,  $N$ , generally increases with increasing  $\Delta$ , consistent with the expected reduction in

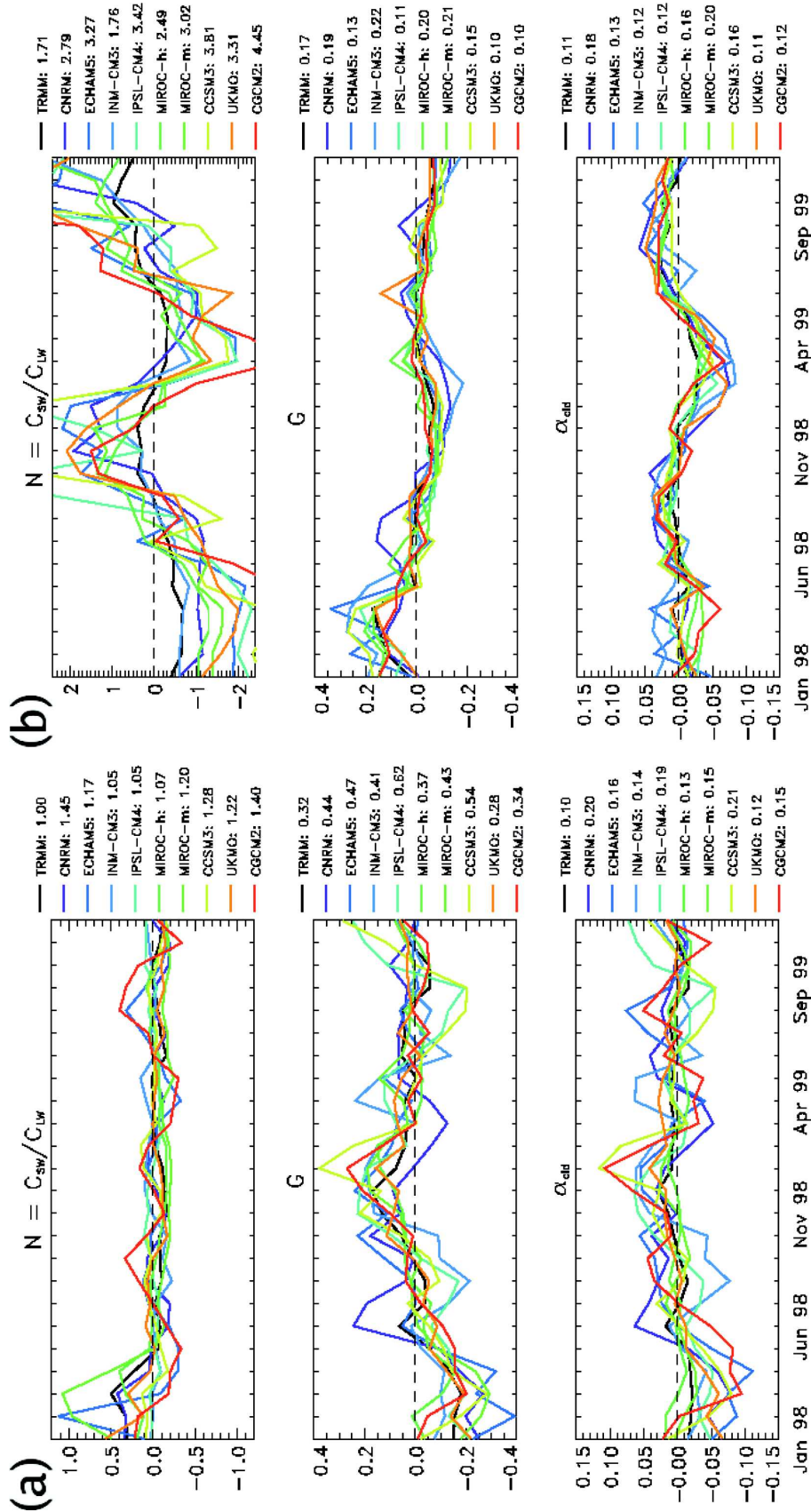


FIG. 8. As in Fig. 6, but for three measures of the influence of clouds on atmospheric radiation balance: (top) the ratio of TOA cloud forcings,  $N$ , and the cloud impact on (middle) greenhouse parameter,  $G$ , and (bottom) albedo,  $\alpha$ .

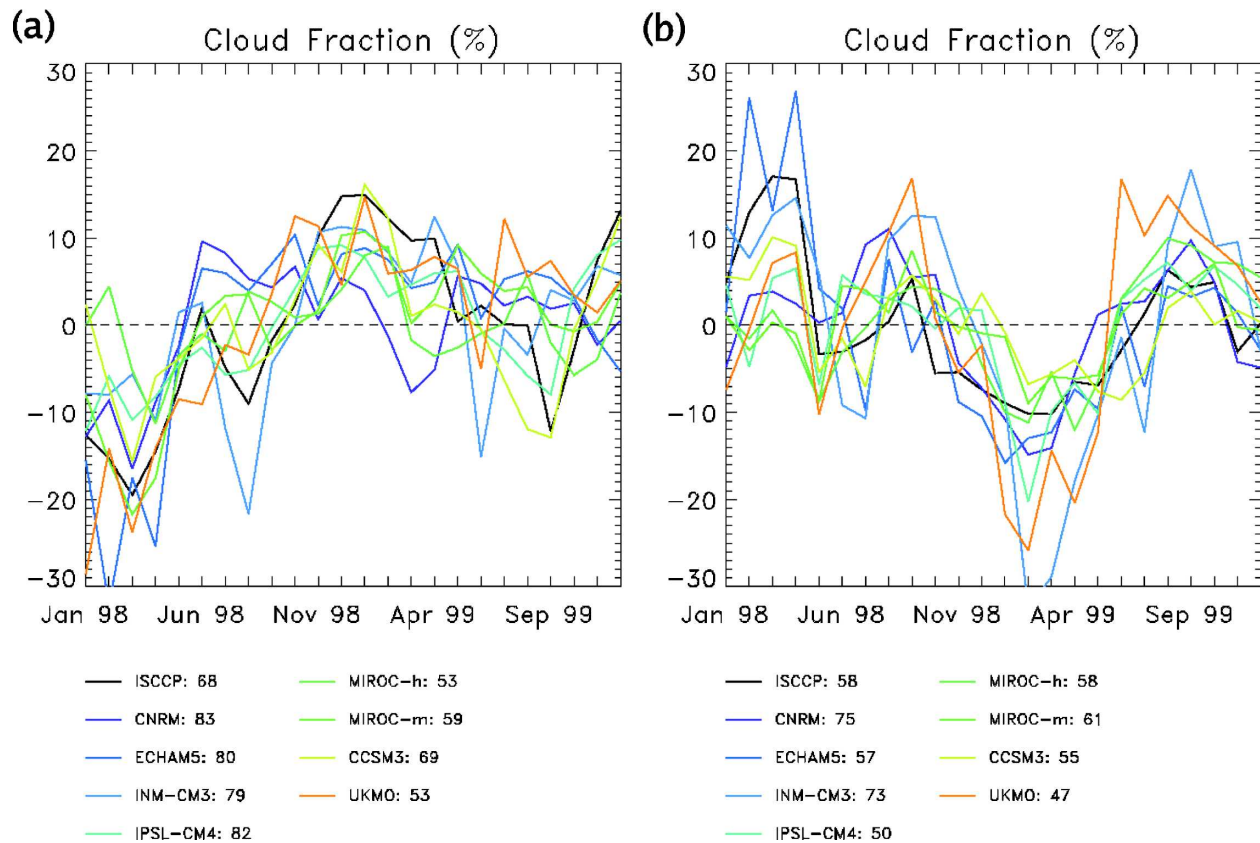


FIG. 9. Monthly mean ISCCP cloud fraction and that predicted by the IPCC AR4 GCMs from January 1998 through December 1999 in the (a) TWP and (b) TEP regions. Mean values over the full period are summarized in the legend.

high cloudiness associated with the subsidence typically observed during periods of normal east–west SST gradients. However, while all sources agree that  $N \approx 1$  during El Niño, the rate of increase with increasing  $\Delta$  varies, suggesting inconsistencies in the response of the vertical organization of clouds between models.

In the TWP, TRMM observations indicate a marked increase in  $N$  during the four months of small east–west SST gradients. Of the four models shown, however, only the CNRM model appears to capture a similar trend, although it also predicts much larger  $N$  at all  $\Delta$  than is observed by TRMM. Relationships between other parameters are equally uncertain among the models. TWP rainfall, for example, is observed to increase with increasing  $\Delta$ . This trend is captured to varying degrees in three of the models, but the INM CM3 predicts an opposite trend entirely. These observations are quantified in Table 6 where the parameters of linear fits of the form  $y = a + b\Delta$  are summarized for rainfall and cloud impact on the greenhouse parameter. These fits, also displayed in Figs. 10 and 11, are not intended to imply that the underlying physical relationship between variables is necessarily linear, but rather to pro-

vide a tool for quantifying similarities and differences between observed relationships and those predicted by the models. In most cases the deviation from linearity in the data is significantly smaller than differences between datasets, allowing conclusions to be drawn without adopting more complicated nonlinear functional relationships that may be more difficult to interpret.

While a majority of the models tend to agree that rainfall in the TWP decreases with decreasing  $\Delta$ , consistent with TRMM observations, the slopes vary widely between them. Furthermore, the strength of the correlation between rainfall and  $\Delta$  varies from less than 0.2 to almost 0.7 between models. The most significant outlier from the group is the INM CM3, which actually predicts precipitation in the TWP region increases slightly during El Niño. It should be noted that all of the datasets exhibit a significant amount of scatter about the best-fit lines. This is to be expected since the east–west SST gradient is primarily driven by SST changes in the TEP region, while the SST in the TWP remains more or less constant throughout the 2-yr period. It is nevertheless disturbing that the disagreement is so large between models and that only two predict slopes

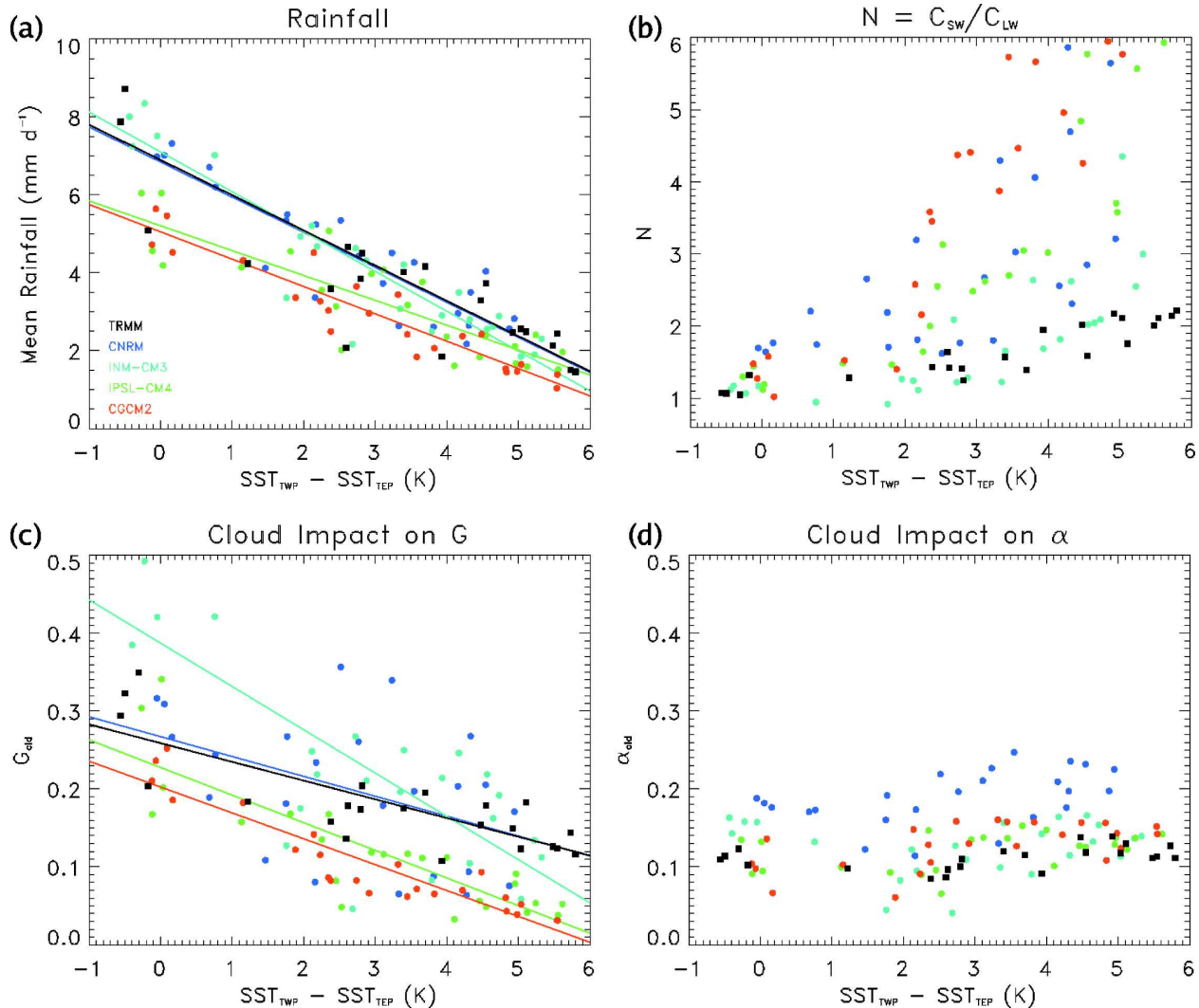


FIG. 10. Observed and modeled influence of the east-west tropical SST gradients on (a) rainfall, (b)  $N$ , (c) cloud impact on  $G$ , and (d) cloud impact on  $\alpha$  in the TEP. The independent variable, defined as the difference in monthly mean SSTs between the TWP and TEP regions, is a proxy for ENSO phase. TRMM observations are identified by filled black squares, while model output is represented by filled circles with colors given in the legend. Also shown are linear fits to the data for selected parameters.

within 20% of that observed by TRMM, given the intensity of the 1998 El Niño event.

The agreement between models and measurements is significantly better in the TEP region. All datasets examined agree that there is a significant increase in precipitation in the TEP as the SST gradient between TWP and TEP decreases. Furthermore, more than half of the models predict slopes within about 15% of the observed  $-0.9 \text{ mm h}^{-1} \text{ K}^{-1}$ . Observed and predicted correlations are in excellent agreement ranging from  $-0.86$  to  $-0.94$  without exception. There is also evidence that the prescribed linear relationship between  $\Delta$  and rainfall fits the data very well in the TEP with mean rms differences on the order of half those for similar fits

in the TWP. There is also a consensus regarding the trends of cloud radiative impacts in the TEP region. Both GCM output and TRMM observations predict that  $N$  decreases substantially during El Niño with values nearing unity corresponding to a near cancellation of LW and SW impacts on TOA radiation. Similarly, all datasets support the fact that cloud impacts on  $G$  increase during El Niño but the amplitude of this trend varies by nearly a factor of 3 between models, as shown in Table 6. Furthermore, while there is agreement that cloud impacts on  $\alpha$  in the TEP do not depend strongly on  $\Delta$ , the mean value varies by a factor of 2 between models. Comparison with Fig. 9 provides more specific insight into the sources of these differences. The

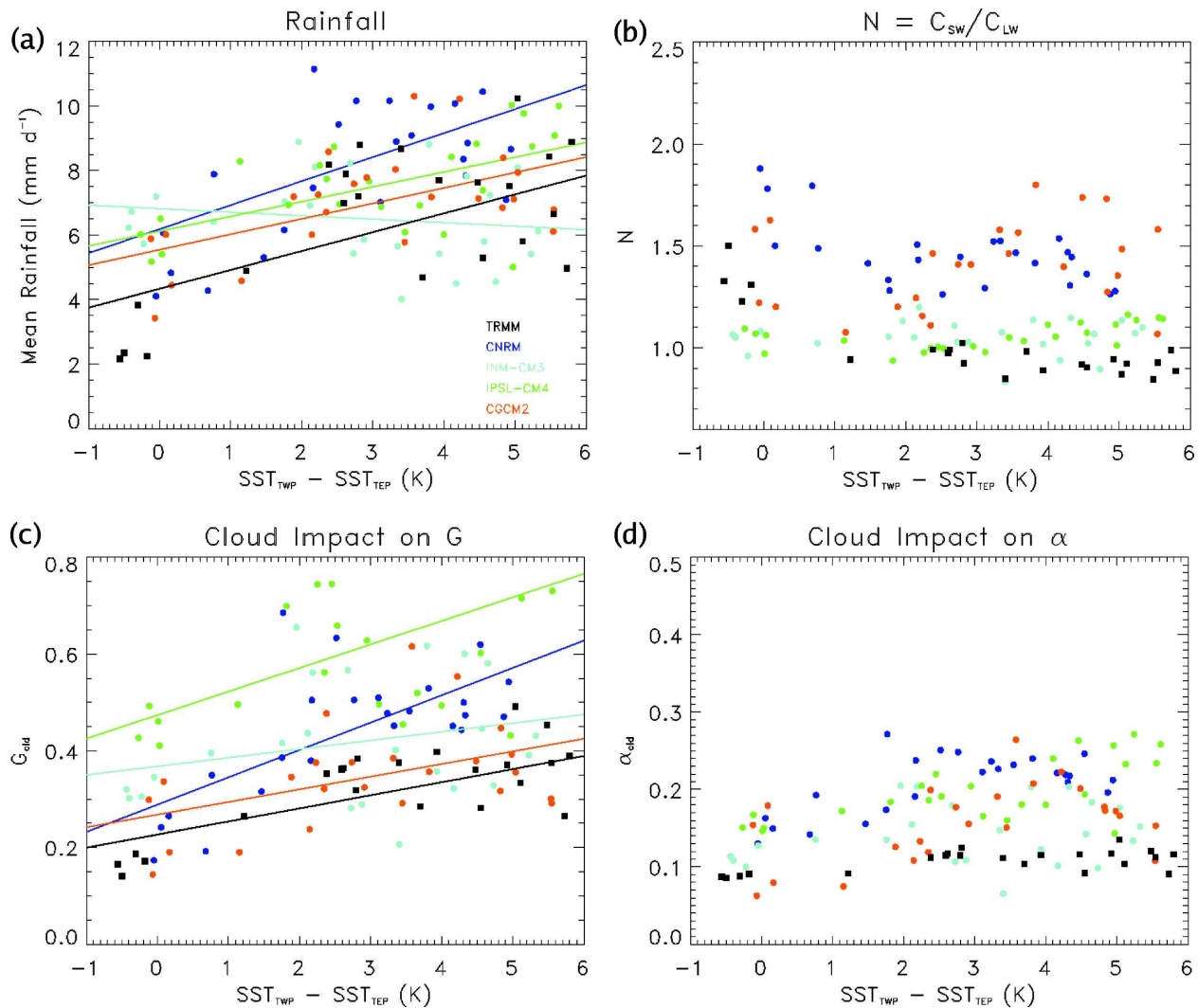


FIG. 11. As in Fig. 10, but for the TWP region.

CCSM3, for example, demonstrates the best agreement with TRMM-derived cloud impact on  $G$  but overestimates cloud impacts on  $\alpha$ , and especially  $N$  under typical SST gradients. Since total cloud amount agrees reasonably well with observations, this suggests that CCSM3 overpredicts the number of low-topped clouds and cloud albedo. Conversely, the INM CM3 overestimates cloud impacts on  $G$  and underestimates  $N$  except during El Niño, while overestimating total cloud amount relative to ISCCP. This indicates that the model underestimates the reduction of high clouds associated with colder SSTs in normal and La Niña periods.

The TWP region provides strong indications of the challenges of correctly representing cloud radiative impacts in GCMs. In most cases models predict that cloud impacts on  $G$  decrease during El Niño, but the overall

magnitude varies by a factor of 2 between models. Similar variability is observed in  $N$  and  $\alpha_{\text{cld}}$ , and most models seem to systematically overestimate both parameters. These results are consistent with the findings of Groisman et al. (2000), Kleeman et al. (2001), Allen et al. (2002), and, most recently, Weare (2004) that all point to deficiencies in the representation of clouds in GCMs from a wide range of different perspectives. Weare, for example, notes that models tend to underestimate cloud overlap with respect to satellite and ground-based observations, an error that is consistent with overestimating cloud radiative effects. Furthermore, the overestimation of cloud impacts on  $G$  by models such as the IPSL CM4 is consistent with the deviations from observed LW cooling in the TWP, in Fig. 5, that occurs during both El Niño and La Niña conditions. It should be noted that differences in the

TABLE 6. Linear fit coefficients for the relationships between surface rainfall ( $\text{mm h}^{-1}$ ) and cloud impact on greenhouse parameter (dimensionless) and  $\Delta = \text{SST}_{\text{TWP}} - \text{SST}_{\text{TEP}}$  (K) including those presented in Figs. 10 and 11. The first two columns,  $a$  and  $b$ , provide the  $y$  intercept and slope, respectively. The third provides the correlation  $r$  between parameters and the last presents the rms difference between fit and data.

Source	$R$ vs $\Delta$				$G$ vs $\Delta$			
	$a$	$b$	$r$	Rms	$a$	$b$	$r$	Rms
Tropical west Pacific								
TRMM	4.3	0.59	0.58	1.9	0.23	0.03	0.67	0.07
CNRM	6.2	0.74	0.52	2.0	0.29	0.06	0.68	0.10
ECHAM5	5.9	1.04	0.68	2.2	0.28	0.06	0.73	0.11
INM CM3	6.8	-0.11	-0.15	1.4	0.37	0.02	0.27	0.12
IPSL CM4	6.1	0.46	0.58	1.3	0.47	0.05	0.59	0.13
MIROC-h	6.1	0.08	0.19	0.9	0.32	0.02	0.46	0.06
MIROC-m	5.3	0.61	0.63	1.4	0.30	0.05	0.69	0.09
CCSM3	6.8	0.25	0.32	1.4	0.43	0.04	0.46	0.15
UKMO	4.7	0.47	0.52	1.5	0.17	0.04	0.73	0.07
CGCM2	5.5	0.48	0.54	1.4	0.27	0.03	0.44	0.10
Tropical east Pacific								
TRMM	6.9	-0.90	-0.87	1.18	0.26	-0.02	-0.83	0.04
CNRM	6.9	-0.90	-0.89	0.73	0.27	-0.03	-0.45	0.08
ECHAM5	6.8	-1.18	-0.88	1.23	0.28	-0.04	-0.77	0.07
INM CM3	7.1	-1.02	-0.92	0.78	0.39	-0.06	-0.79	0.08
IPSL CM4	5.2	-0.64	-0.86	0.73	0.23	-0.04	-0.84	0.04
MIROC-h	6.3	-0.69	-0.93	0.52	0.32	-0.04	-0.93	0.03
MIROC-m	6.1	-0.73	-0.88	0.71	0.34	-0.05	-0.89	0.04
CCSM3	6.0	-1.03	-0.95	0.65	0.30	-0.05	-0.82	0.06
UKMO	7.0	-0.96	-0.86	1.05	0.18	-0.02	-0.64	0.05
CGCM2	5.1	-0.70	-0.94	0.47	0.20	-0.03	-0.93	0.03

magnitude of  $G_{\text{clid}}$  and  $\alpha_{\text{clid}}$  have important implications for the magnitude of cloud–radiation feedbacks. An increase in high clouds consistent with a large value of  $G_{\text{clid}}$  can be expected to exert a stabilizing influence on the environment by introducing heating in the upper troposphere. Similarly, to first order, large cloud impacts on  $\alpha$  have a cooling influence on the SST by reducing the amount of solar radiation that reaches the surface. Uncertainties in the way models represent cloud radiative impacts and, in particular, their sensitivity to ENSO translate into large differences in their estimates of the magnitude of cloud radiative feedbacks. The large intermodel variability in the TWP region may, therefore, be indicative of substantial differences in the strength of cloud–radiative feedbacks among GCMs that are likely not limited to the ENSO cycle analyzed here but to other climate change scenarios as well.

As noted in sections 3 and 4, the observed differences in net heating in the east and west Pacific between El Niño and La Niña conditions suggest a fundamental change in atmospheric heat transport that implies a corresponding shift in the large-scale circulation pattern across the Pacific. This implies that large-scale vertical motion in the region must also exhibit a response to the 1998 El Niño event. In light of the studies of Fu et al.

(1990), Lau et al. (1997), and Bony et al. (1997) that suggest that cloud radiative impacts are strongly connected to large-scale circulation patterns, the behavior of modeled vertical motion fields warrants some discussion even though direct satellite observations do not exist for comparison. Figure 12 presents the response of 500-mb vertical motion in the TEP and TWP regions to the east–west SST gradient,  $\Delta$ . Again, four models that span the range of behavior of the ensemble are isolated for clarity. As with previous variables the agreement between models is much better in the TEP region where the strength of the SST forcing on local dynamics is strongest. Subsidence is generally reduced in periods of reduced east–west SST gradient, and the slopes of the trends are qualitatively similar. In the TWP, there is a general trend toward deeper large-scale ascent as  $\Delta$  increases, but the models disagree widely as to the strength of this trend. The INM CM3, for example, indicates that  $\omega_{500}$  exhibits only a very weak sensitivity, while the CNRM model indicates a strong coupling between vertical motion and east–west SST gradient sufficient to actually reverse the sign of large-scale vertical motion during the intense 1998 El Niño.

Thus a consistent picture emerges in which many of the IPCC AR4 GCMs underrepresent the sensitivities of clouds, precipitation, atmospheric heating, and the

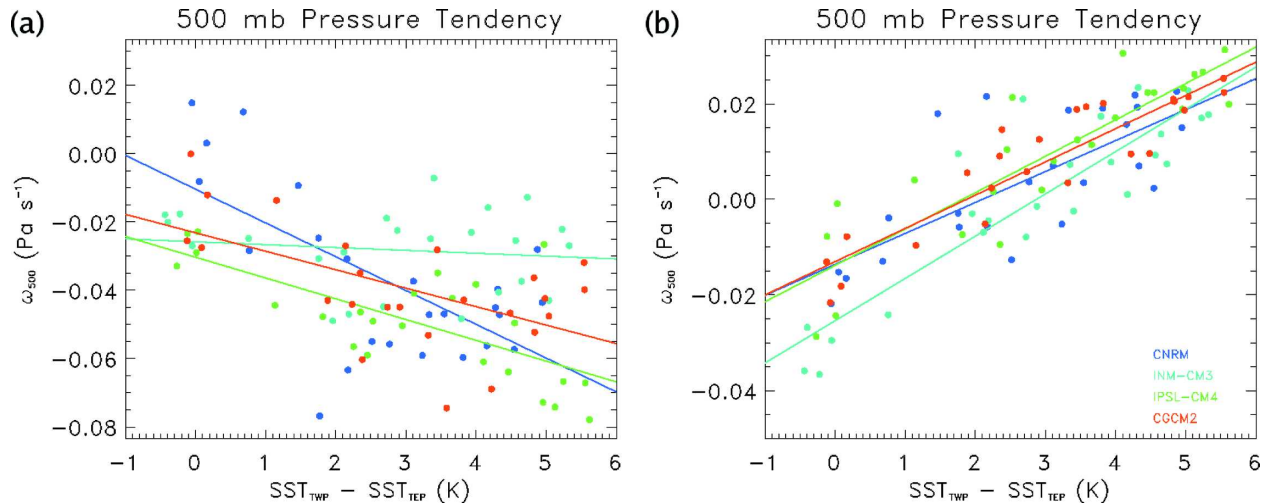


FIG. 12. Modeled relationships between 500-mb pressure tendency and  $\Delta$  in (a) the TWP and (b) the TEP.

strength of the zonal Walker circulation to El Niño, especially in the TWP. In short, while the local atmospheric response to warmer SSTs is generally captured (as in the TEP), models fail to represent teleconnections to neighboring regions (such as the TWP) that are observed to be connected through large-scale dynamics. This misrepresentation of the atmospheric response to a systematic change in the underlying forcing has serious implications for longer-term climate change, particularly given the importance of the TWP region in the global energy and water cycles.

## 6. Conclusions

With the growing need to simulate future climate conditions and the relatively short climate record supplied by satellite observations, climate models provide an invaluable tool for studying the potential impacts of human activities on the environment. As one seeks to resolve smaller signals, such as those associated with short-term climate change, regional processes become increasingly important, requiring a rigorous evaluation of simulated changes in local energy and water cycles, particularly since model output is being leveraged to continuously increasing degrees in developing global environmental policy. This study makes use of visible, infrared, and microwave radiance measurements from the sensors aboard TRMM to evaluate the sensitivity of atmospheric heating and the factors that modify it to changes in east–west SST gradients associated with ENSO in the IPCC AR4 GCMs.

Nearly all of the models examined yield annual-mean atmospheric energy budgets across the equatorial Pacific that agree with satellite-based estimates to within

observational error bounds. Analysis of smaller spatial scales and shorter time periods, however, reveals deficiencies in their representation of the response of atmospheric heating to the 1998 El Niño event. While the models predict very similar trends in water vapor, precipitation, and large-scale vertical motion in the east Pacific where the changes in local SST are large, a majority of models fail to capture the observed atmospheric cooling and large-scale subsidence in the west Pacific during the 1998 El Niño, primarily due to a significant overestimation of the amount of latent heat released in precipitation. Since changes in SST are comparatively small in this region, responses of atmospheric properties to ENSO must be driven primarily by changes in the large-scale circulation pattern across the equatorial Pacific associated with differences in east–west SST gradients. The findings suggest that this less direct relationship to local SST poses a challenge to climate models, leading to an overall lack of consensus among the nine GCMs examined.

Many models also misrepresent the radiative impacts of clouds in both regions, implying errors in total cloudiness, cloud thickness, and the relative frequency of occurrence of high and low clouds. As a result, cloud impacts on LW radiative heating and planetary albedo are overestimated in many of the models examined. Given intermodel differences in cloud amount that exceed 30%, significant variability in the predicted amplitudes of the responses of both LW and SW cloud impacts to ENSO, and the apparent systematic biases between modeled and measured cloud impacts, it is reasonable to conclude that the representation of clouds in GCMs remains a large source of uncertainty in the IPCC AR4 GCMs, limiting their predictive skill

when simulating the impacts of SST changes on regional atmospheric energy and water cycles. In light of studies such as that of Lee et al. (2001), who find that the propagation speed of intraseasonal oscillations in GCMs is a strong function of the ratio of radiative to latent heating governed by the autoconversion time scale between clouds to precipitation, and those of Slingo and Slingo (1988, 1991), who demonstrate the importance of cloud–radiation interactions in defining the strength of the meridional and zonal circulations, these errors have important implications for simulating processes on a wide range of space–time scales. As a result, it is reasonable to expect that the IPCC AR4 GCMs also exhibit a wide range in the strengths of cloud–radiation–precipitation feedbacks in longer-term simulations that seek to predict the effects of increasing CO<sub>2</sub> concentrations on future climate.

This study highlights the importance of accurate, global, multiparameter energy and water cycle datasets for providing tight constraints on climate models on a variety of spatial and temporal scales. While the 1998 El Niño event provides a useful source of natural climate variability for assessing the coupling between the energy and water cycles in climate models, it must be emphasized that this is a single event. Both model and observational datasets will not only exhibit signals related to the underlying SST fields, but also a significant amount of noise that can only be reduced by compositing the responses over multiple ENSO events. Improved datasets spanning longer periods and integrating advanced technologies, such as those on the A-Train constellation, will ultimately be required to more completely evaluate the parameterized physics employed in GCMs and, ultimately, to refine these parameterizations for future generations of models. Such advances will be necessary in order to more accurately represent the coupling between the energy and water cycles in developing a complete theory of global climate change.

*Acknowledgments.* Financial support for this research was provided, in part, by NASA Energy and Water Cycle Sponsored (NEWS) Research Grant NNG06GC46G and by NASA Research Grant NNG04GB97G. We acknowledge the international modeling groups for providing their data for analysis, the Program for Climate Model Diagnosis and Intercomparison (PCMDI) for collecting and archiving the model data, the JSC/CLIVAR Working Group on Coupled Modelling (WGCM) and their Coupled Model Intercomparison Project (CMIP) and Climate Simulation Panel for organizing the model data analysis activity, and the IPCC WG1 TSU for technical support. The

IPCC Data Archive at Lawrence Livermore National Laboratory is supported by the Office of Science, U.S. Department of Energy. TRMM data were acquired through the Goddard Distributed Active Archive Center at the Goddard Space Flight Center. Water vapor, SST, and surface wind speed data used are produced by Remote Sensing Systems and sponsored, in part, by NASA's Earth Science Information Partnerships (ESIP): a federation of information sites for earth science; and by the NOAA/NASA Pathfinder Program for early EOS products, whose principal investigator is Frank Wentz. ISCCP data were obtained from the NASA Langley Research Center Atmospheric Science Data Center (<http://eosweb.larc.nasa.gov>).

#### REFERENCES

- Allen, R. P., A. Slingo, and M. A. Ringer, 2002: Influence of dynamics on the changes in tropical cloud radiative forcing during the 1998 El Niño. *J. Climate*, **15**, 1979–1986.
- Bjerknes, J., 1969: Atmospheric teleconnections from the equatorial Pacific. *Mon. Wea. Rev.*, **97**, 163–172.
- Boer, G. J., and Coauthors, 1992: Some results from an intercomparison of the climates simulated by 14 atmospheric general circulation models. *J. Geophys. Res.*, **97**, 12 771–12 786.
- Bony, S., K.-M. Lau, and Y. C. Sud, 1997: Sea surface temperature and large-scale circulation influences on tropical greenhouse effect and cloud radiative forcing. *J. Climate*, **10**, 2055–2077.
- Boyle, J. S., 1998: Intercomparison of interannual variability of the global 200-hPa circulation for AMIP simulations. *J. Climate*, **11**, 2505–2529.
- Cess, R. D., M. Zhang, B. A. Wielicki, D. F. Young, X.-L. Zhou, and Y. Nikitenko, 2001: The influence of the 1998 El Niño upon cloud-radiative forcing over the Pacific warm pool. *J. Climate*, **14**, 2129–2137.
- Collins, W. D., and Coauthors, 2006: The Community Climate System Model version 3 (CCSM3). *J. Climate*, **19**, 2122–2143.
- Cooper, S. J., T. S. L'Ecuyer, and G. L. Stephens, 2003: The impact of explicit cloud boundary information on ice cloud microphysical property retrievals from infrared radiances. *J. Geophys. Res.*, **108**, 4107, doi:10.1029/2002JD002611.
- Cornejo-Garrido, A. G., and P. H. Stone, 1977: On the heat balance of the Walker circulation. *J. Atmos. Sci.*, **34**, 1155–1162.
- Deque, M., C. Dreveton, A. Graun, and D. Cariolle, 1994: The ARPEGE/IFS atmosphere model: A contribution to the French community climate modeling. *Climate Dyn.*, **10**, 249–266.
- Eyre, J. R., 1990: The information content of data from satellite sounding systems: A simulation study. *Quart. J. Roy. Meteor. Soc.*, **116**, 401–434.
- , G. A. Kelly, A. P. McNally, E. Anderson, and A. Persson, 1993: Assimilation of TOVS radiance information through one-dimensional variational analysis. *Quart. J. Roy. Meteor. Soc.*, **119**, 1427–1463.
- Fekete, B. M., C. J. Vorosmarty, J. O. Roads, and C. J. Willmott, 2004: Uncertainties in precipitation and their impacts on runoff estimates. *J. Climate*, **17**, 294–304.

- Flato, G. M., cited 2005: The third generation Coupled Global Climate Model (CGCM3). Canadian Centre for Climate Modelling and Analysis, Victoria, BC, Canada. [Available online at <http://www.ccma.bc.ec.gc.ca/models/cgcm3.shtml>.]
- Fu, R., A. D. D. Genio, and W. B. Rossow, 1990: Behavior of deep convective clouds in the tropical Pacific deduced from ISCCP radiances. *J. Climate*, **3**, 1129–1152.
- Gadgil, S., and S. Sajani, 1998: Monsoon precipitation in the AMIP runs. *Climate Dyn.*, **14**, 659–689.
- Galini, V. Y., E. M. Volodin, and S. P. Smyshliaev, 2003: Atmospheric general circulation model of INM RAS with ozone dynamics. *Russ. Meteor. Hydrol.*, **5**, 13–22.
- Gates, W. L., 1992: AMIP: The Atmospheric Model Intercomparison Project. *Bull. Amer. Meteor. Soc.*, **73**, 1962–1970.
- , and Coauthors, 1999: An overview of the results of the Atmospheric Model Intercomparison Project (AMIP I). *Bull. Amer. Meteor. Soc.*, **80**, 29–55.
- Glecker, P. J., 1996: *AMIP Newsletter*. No. 8, PCMDI, Lawrence Livermore National Laboratory, Livermore, CA, 24 pp.
- Gordon, C. C., C. Cooper, C. A. Senior, H. T. Banks, J. M. Gregory, T. C. Johns, J. F. B. Mitchell, and R. A. Wood, 2000: The simulation of SST, sea ice extents, and ocean heat transports in a version of the Hadley Centre coupled model without flux adjustments. *Climate Dyn.*, **16**, 147–168.
- Greenwald, T. J., G. L. Stephens, T. H. Vonder Haar, and D. L. Jackson, 1993: A physical retrieval of cloud liquid water over the global oceans using special sensor microwave/imager (SSM/I) observations. *J. Geophys. Res.*, **98**, 18 471–18 488.
- Groisman, P. Y., R. S. Bradley, and B. Sun, 2000: The relationship of cloud cover to near-surface temperature and humidity: Comparison of GCM simulations with empirical data. *J. Climate*, **13**, 1858–1878.
- Hartmann, D. L., D. A. Short, H. H. Hendon, and R. A. Houze Jr., 1984: Some implications of the mesoscale circulation in tropical cloud clusters for large-scale dynamics and climate. *J. Atmos. Sci.*, **41**, 113–121.
- Hasumi, H., and S. Emori, Eds., 2004: K-1 coupled model (MIROC) description. K-1 Tech. Rep. 1, K-1 Model Developers, Center for Climate System Research, University of Tokyo, Tokyo, Japan, 34 pp. [Available online at <http://www.ccsr.u-tokyo.ac.jp/kyosei/hasumi/MIROC/tech-repo.pdf>.]
- Houze, R. A., Jr., 1982: Cloud clusters and large-scale vertical motions in the tropics. *J. Meteor. Soc. Japan*, **60**, 396–409.
- , 1989: Observed structure of mesoscale convective systems and implications for large-scale heating. *Quart. J. Roy. Meteor. Soc.*, **115**, 425–461.
- Julian, P. R., and R. M. Chervin, 1978: A study of the Southern Oscillation and Walker Circulation phenomenon. *Mon. Wea. Rev.*, **106**, 1433–1451.
- Kharin, V. V., F. W. Zwiers, and X. Zhang, 2005: Intercomparison of near-surface temperature and precipitation extremes in AMIP-2 simulations, reanalyses, and observations. *J. Climate*, **18**, 5201–5223.
- Kiehl, J. T., 1994: On the observed near cancellation between longwave and shortwave cloud forcing in tropical regions. *J. Climate*, **7**, 559–565.
- Kleeman, R., G. Wang, and S. Jewson, 2001: Surface flux response to interannual tropical Pacific sea surface temperature variability in AMIP models. *Climate Dyn.*, **17**, 627–641.
- Kummerow, C., and Coauthors, 2000: The status of the Tropical Rainfall Measuring Mission (TRMM) after two years in orbit. *J. Appl. Meteor.*, **39**, 1965–1982.
- Lau, K.-M., and L. Peng, 1987: Origin of low-frequency (intraseasonal) oscillations in the tropical atmosphere. Part I: Basic theory. *J. Atmos. Sci.*, **44**, 950–972.
- , J. H. Kim, and Y. Sud, 1996: Intercomparison of hydrologic processes in AMIP GCMs. *Bull. Amer. Meteor. Soc.*, **77**, 2209–2227.
- , H.-T. Wu, and S. Bony, 1997: The role of large-scale atmospheric circulation in the relationship between tropical convection and sea surface temperature. *J. Climate*, **10**, 381–392.
- L'Ecuyer, T., and G. L. Stephens, 2002: An uncertainty model for Bayesian Monte Carlo retrieval algorithms: Application to the TRMM observing system. *Quart. J. Roy. Meteor. Soc.*, **128**, 1713–1737.
- , and —, 2003: The tropical oceanic energy budget from the TRMM perspective. Part I: Algorithm and uncertainties. *J. Climate*, **16**, 1967–1985.
- , H. Masunaga, and C. Kummerow, 2006: The characteristics of tropical precipitation systems. Part II: Radiative properties. *J. Climate*, **19**, 1388–1406.
- Lee, M.-I., I.-S. Kang, J.-K. Kim, and B. E. Mapes, 2001: Influence of cloud-radiation interaction on simulating tropical intraseasonal oscillation with an atmospheric general circulation model. *J. Geophys. Res.*, **106**, 14 219–14 233.
- Mao, J., and A. Robock, 1998: Surface air temperature simulations by AMIP general circulation models: Volcanic and ENSO signals and systematic errors. *J. Climate*, **11**, 1538–1552.
- Mapes, B. E., and R. A. Houze Jr., 1995: Diabatic divergence profiles in western Pacific mesoscale systems. *J. Atmos. Sci.*, **52**, 1807–1828.
- Marti, O., and Coauthors, 2005: The new IPSL climate system model: IPSL-CM4. Note du Pole de Model 26, Institut Pierre Simon Laplace des Sciences de l'Environnement Global, Paris, France, 86 pp. [Available online at <http://dods.ipsl.jussieu.fr/omamce/IPSLCM4/DocIPSLCM4/FILES/DocIPSLCM4.pdf>.]
- Reynolds, R. W., and T. M. Smith, 1994: Improved global sea surface temperature analyses. *J. Climate*, **7**, 929–948.
- Roeckner, E., 2003: The atmospheric general circulation model ECHAM5. Part I: Model description. MPI Rep. 349, Max-Planck-Institut Für Meteorologie, Hamburg Germany, 127 pp.
- Rossow, W. B., and R. A. Schiffer, 1991: ISCCP cloud data products. *Bull. Amer. Meteor. Soc.*, **72**, 2–20.
- , and —, 1999: Advances in understanding clouds from ISCCP. *Bull. Amer. Meteor. Soc.*, **80**, 2261–2288.
- Sherwood, S. C., V. Ramanathan, T. P. Barnett, M. K. Tyree, and E. Roeckner, 1994: Response of an atmospheric general circulation model to radiative forcing of tropical clouds. *J. Geophys. Res.*, **99**, 20 829–20 845.
- Slingo, A., and J. M. Slingo, 1988: The response of a general circulation model to cloud longwave radiative forcing. I: Introduction and initial experiments. *Quart. J. Roy. Meteor. Soc.*, **114**, 1027–1062.
- Slingo, J. M., and A. Slingo, 1991: The response of a general circulation model to cloud longwave radiative forcing. II: Further studies. *Quart. J. Roy. Meteor. Soc.*, **117**, 333–364.
- Soden, B. J., 2000: The sensitivity of the tropical hydrological cycle to ENSO. *J. Climate*, **13**, 538–549.

- Sperber, K. R., and T. N. Palmer, 1996: Interannual tropical rainfall variability in general circulation model simulations associated with the Atmospheric Model Intercomparison Project. *J. Climate*, **9**, 2727–2750.
- Srinivasan, G., M. Hulme, and C. G. Jones, 1995: An evaluation of the spatial and interannual variability of tropical precipitation as simulated by GCMs. *Geophys. Res. Lett.*, **22**, 2139–2142.
- Stephens, G. L., and T. J. Greenwald, 1991: The Earth's radiation budget and its relation to atmospheric hydrology: 2. Observations of cloud effects. *J. Geophys. Res.*, **96**, 15 325–15 340.
- Weare, B. C., 2004: A comparison of AMIP II model cloud layer properties with ISCCP D2 estimates. *Climate Dyn.*, **22**, 281–292.
- Wentz, F., 1997: A well-calibrated ocean algorithm for Special Sensor Microwave/Imager. *J. Geophys. Res.*, **102**, 8703–8718.
- Wielicki, B. A., B. R. Barkstorm, E. F. Harrison, R. B. Lee III, G. L. Smith, and J. E. Cooper, 1996: Clouds and the Earth's Radiant Energy System (CERES): An Earth Observing System experiment. *Bull. Amer. Meteor. Soc.*, **77**, 853–868.
- Wild, M., C. N. Long, and A. Ohmura, 2006: Evaluation of clear-sky solar fluxes in GCMs participating in AMIP and IPCC-AR4 from a surface perspective. *J. Geophys. Res.*, **111**, D01104, doi:10.1029/2005JD006118.